Journal of Materials Research and Technology 39 (2025) 5597–5611

Contents lists available at ScienceDirect

Journal of Materials Research and Technology

journal homepage: www.elsevier.com/locate/jmrt

DED-LB manufactured Ti–6Al–4V–4Cu alloy: materials development, characterization, and *in vivo* biocompatibility

Andrej Jeromen [a], Anish Nair [a], Peter Rodič [b], Denis Sačer [b], Barbara Kapun [b], Maša Čater [c], Ana Brunčić [c], Katarina Kozlica [d], Radmila Milačič Ščančar [d], Andrej Cör [e], Edvard Govekar [a,***], Ingrid Milošev [b,e,**], Simon Horvat [c,*]

[a] University of Ljubljana, Faculty of Mechanical Engineering, Aškerčeva c. 6, SI-1000, Ljubljana, Slovenia
[b] Jožef Stefan Institute, Department of Physical and Organic Chemistry, Jamova c. 39, SI-1000, Ljubljana, Slovenia
[c] University of Ljubljana, Biotechnical Faculty, Department of Animal Science, Groblje 3, 1230, Domžale, Slovenia
[d] Jožef Stefan Institute, Department of Environmental Sciences, Jamova c. 39, SI-1000, Ljubljana, Slovenia
[e] Valdoltra Orthopaedic Hospital, Jadranska c. 31, SI-6280, Ankaran, Slovenia

ARTICLE INFO

Handling Editor: P.Y. Chen

Keywords:
Ti–6Al–4V–4Cu alloy
Additive manufacturing
Laser-based directed energy deposition (DED-LB)
Microstructure and phase analyses
Corrosion
In vivo biocompatibility

ABSTRACT

This study investigates the fabrication, characterization and biocompatibility of a Ti–6Al–4V–4Cu alloy produced from spherical Ti–6Al–4V and Cu powders using the directed energy deposition (DED-LB) process with an annular laser beam (ALB). Based on process stability related wall rectangularity, and interlayer bonding, the optimal build strategy of the wall samples was achieved by a bi-directional path with reducing ALB power and initial power of 1250 W. Microstructural characterization included optical microscopy for grain morphology, SEM with analysis for microstructure and elemental distribution, and XRD for phase identification. Electrochemical performance was assessed in a simulated physiological environment, demonstrating passive behavior and corrosion resistance. To evaluate *in vivo* biocompatibility, disc-shaped implants were inserted subcutaneously in mice and monitored for physiological, hematological, biochemical, and histological responses over a period of 7 or 56days. Mice exhibited no signs of adverse effects with stable feed and water intake, normal body weight, and typical behavior. Hematological and metabolic profiles revealed no significant differences between the Ti–6Al–4V–4Cu, Ti–6Al–4V, sham, and untreated groups. Histological analysis revealed that the implants were well-integrated with surrounding tissues, with no evidence of granulomatous inflammation, immune cell infiltration, or abnormal tissue morphology. ICP-MS analysis of the mouse serum revealed stable concentrations of Cu, Al, V, and Ti, indicating no systemic metal release. These findings confirm that DED-LB fabricated Ti–6Al–4V–4Cu alloy exhibits favorable *in vivo* biocompatibility and systemic safety in mice. The results support its potential for biomedical applications that require corrosion resistance and biocompatibility, and warrant further *in vivo* evaluation of its antibacterial properties.

1. Introduction

Implants are widely used in medicine to repair damaged bones, replace joints or teeth, or support healing after injury. The functionality and longevity of these implants are highly dependent on the materials used in their manufacture. Titanium alloys, particularly Ti–6Al–4V, are among the most widely used materials for the manufacture of implants. Ti–6Al–4V is known for its high strength, low weight, corrosion resistance, and good biocompatibility [1–3]. However, implant-related infections affecting 1–5 % of patients remain a major clinical problem that can hinder recovery or even necessitate revision surgery [4]. Recent reviews also highlight the growing focus on tailoring Ti-based alloys, including β-phase stabilized systems, to enhance mechanical compatibility with bone and improve biological performance in orthopedic and dental applications [5].

To address the mitigation of implant-related incidence, there is a

* Corresponding author.
** Co-corresponding author.
*** Co-corresponding author.
E-mail addresses: edvard.govekar@fs.uni-lj.si (E. Govekar), ingrid.milosev@ijs.si (I. Milošev), simon.horvat@bf.uni-lj.si (S. Horvat).

https://doi.org/10.1016/j.jmrt.2025.10.151
Received 19 August 2025; Received in revised form 8 October 2025; Accepted 18 October 2025
Available online 24 October 2025

growing interest in improving the antibacterial and biocompatible properties of implant materials through alloying [6]. One of the various strategies is to alloy with copper (Cu), which has documented antibacterial properties as it disrupts bacterial cell membranes, leading to cell death [7]. Alloying Ti–6Al–4V with Cu produces a microstructure consisting of titanium α-phase and β-phase, along with intermetallic Ti_2Cu phase, which can potentially provide the antibacterial effect [8]. The Ti–6Al–4V–*x*Cu alloy has already shown promise in delivering antibacterial function without compromising mechanical integrity or biocompatibility [9–11]. Recent reviews emphasize that Ti–Cu alloys represent a promising class of next-generation biomaterials due to their combined antibacterial efficacy, enhanced corrosion resistance, and tunable mechanical properties. These are all attributes that are strongly influenced by the distribution and morphology of the Ti_2Cu phase, which are shaped by processing methods [12,13].

The first attempts to develop Ti–6Al–4V–*x*Cu alloys were primarily based on conventional manufacturing technologies, such as casting and powder metallurgy [14,15]. However, these methods often lead to heterogeneous microstructures and a non-uniform distribution of the Ti_2Cu phase [8], resulting in reduced antibacterial performance and mechanical brittleness [10,16]. In addition, conventional methods are associated with challenges due to the high melting point of titanium and its reactivity with oxygen, as well as the reduced ability to produce complex, customized shapes.

In this context, additive manufacturing (AM) has emerged as a promising alternative to conventional manufacturing technologies, offering significant advantages in terms of design freedom, material utilization, and ability to tailor the microstructure. AM processes enable the layer-by-layer construction of complex, personalized implants directly from digital models, reducing material waste and production lead times. For Ti–6Al–4V-*x*Cu alloys, AM offers the added benefit of precise control over the incorporation and distribution of Cu, which is critical for improving antibacterial functionality while maintaining desirable mechanical properties.

Among the AM processes, laser-based powder bed fusion (PBF-LB) [17] has been extensively used for the fabrication of Ti–6Al–4V–*x*Cu alloys with 1–15 wt% Cu [18–20]. In addition, Ti–6Al–4V–*x*Cu alloys produced with PBF-LB have been shown to have better mechanical properties and higher antibacterial activity compared to alloys produced with conventional technologies [21]. However, the concentrated energy input and extreme cooling rate typical of PBF-LB, combined with the large difference between the melting points and thermal conductivities of Ti–6Al–4V and Cu, can lead to segregation of the elements, vaporization of Cu powder particles, and, similar to conventional manufacturing, non-uniform Ti_2Cu phase formation [22,23]. Limited build volume and relatively low deposition rate are also limiting factors in the PBF-LB process for use in implant manufacturing. Furthermore, the development of such complex alloys demands multi-material capability, which in the case of PBF-LB remains at an early stage of development, constrained by process control and system design challenges (powder switching, recoater design, cross-contamination, etc.) and complex build strategies [24–26].

To overcome these limitations of PBF-LB, another established AM process, laser beam directed-energy deposition (DED-LB), can be used. DED-LB utilizes a higher power and significantly larger laser beam diameter, along with lower scanning speeds compared to PBF-LB, which considerably reduces the risk of Cu vaporization. In addition, the slower cooling rate of the DED-LB deposited material promotes the formation of fine intermetallic Ti_2Cu phases, which are desirable [27]. For the DED-LB fabrication of Ti–Cu alloys, both wire [28] and powder feedstock [27] have already been successfully used. However, the wire-fed approach is limited by its reliance on pre-alloyed wires, which restricts flexibility in customizing the composition of the deposited material. In addition, the DED-LB encounters several challenges, such as lower spatial resolution, limited surface finish quality, and difficulties in achieving precise control over sharp interfaces. Nevertheless, for the development of Ti–6Al–4V–Cu alloys, powder-based DED-LB offers notable advantages over PBF-LB, primarily due to its ability for versatile multi-material fabrication - including mixing of powders in precise ratios and switching of feedstocks in real time, enabling the production of alloys with well-defined material compositions and tailored properties [29–31]. However, there are few published results on the fabrication of Ti–Cu alloys with powder DED-LB. Nevertheless, the significant antibacterial properties of the powder DED-LB fabricated Ti–Cu alloy have been demonstrated through the effective inhibition of bacterial growth [27], as well as improved mechanical properties and uniformity of Ti_2Cu phase distribution [32]. Furthermore, the addition of Cu to Ti–6Al–4V in powder DED-LB [33] was reported to result in refined grains, a uniform composition, enhanced strength and hardness compared to the deposited Ti–6Al–4V. Despite these promising results, significant knowledge gaps remain in powder DED-LB fabrication of Ti–6Al–4V-*x*Cu alloys, particularly regarding material microstructure and biocompatibility. This is also applicable to the corrosion resistance of DED-LB-fabricated Ti–6Al–4V-*x*Cu. The high corrosion resistance of metallurgically produced wrought Ti–6Al–4V has been well established in the *in vitro* studies using simulated physiological fluids and long-term clinical practice [34]. The corrosion resistance of Ti–6Al–4V produced by various AM methods has been investigated and generally shown to be comparable to the metallurgically produced alloy, although with some differences, as will be detailed in the text below. Among AM methods, the Ti–6Al–4V samples were most often produced using PBF-LB (also referred to as selective laser melting, SLM) [35–46], whereas electron beam melting (EBM) [36,47] or DED-LB [48] were used more sparingly. In our previous work [49], we investigated the corrosion resistance of Ti–6Al–4V alloy produced by DED-LB and compared it to that of the wrought alloy. Regarding the corrosion and electrochemical properties of AM-produced Ti metal and Ti–6Al–4V alloys with the addition of copper, mostly those produced by PBF-LF methods have been investigated, i.e. Ti–5Cu [50–52] and Ti–6Al–4V–*x*Cu alloys [20,53–55]. However, the effect of copper addition on electrochemical and corrosion properties of Ti alloys has been much less addressed when using DED [27].

A number of studies have explored the antibacterial properties and biocompatibility of copper-containing alloys, primarily through *in vitro* assays, and a selection of these publications is presented here. Investigation of Ti–6Al–4V alloys with varying Cu contents demonstrated enhanced antibacterial activity against *E. coli* and *S. aureus*, along with satisfactory cytocompatibility [55]. Guo and Lin (2017) [20] evaluated Ti–Cu alloys prepared by selective laser melting for antibacterial activity against *S. aureus*. Alloys with 3–5 wt% Cu achieved >99.9 % bacterial reduction within 24 h. In a study of Zhang et al. (2016) [56], Ti–Cu sintered alloys were evaluated for antibacterial activity against *S. aureus* using an *in vitro* plate-counting method. Alloys with ≥5 wt% Cu achieved over 99 % bacterial reduction, attributed to the release of copper ions. Ti–Cu alloys fabricated by PBF-LB exhibited significant antibacterial efficiency and corrosion resistance [50]. The combination of nanoscale surface roughness with Cu addition further enhanced antibacterial performance against *S. aureus* without affecting osteoblast viability [57]. Ti–Cu alloys with different Ti_2Cu phase morphologies also improved antibacterial efficacy without compromising cell compatibility in dental applications [58]. In another study, Ti–5Cu alloys modified with plasma achieved over 99 % bactericidal efficiency against *S. aureus* [59], whereas Ti–15Zr–*x*Cu alloys improved antibacterial properties while maintaining bioactivity [60]. Collectively, these *in vitro* investigations highlight the promise of Cu-containing alloys for biomedical applications. However, supporting their future use in biomedicine, caution is warranted when extrapolating these *in vitro* results to *in vivo* or clinical settings. By contrast to several *in vitro* studies, relatively fewer studies have assessed the *in vivo* performance of copper-containing metals and alloys. Sintered Ti–10Cu implants significantly reduced *S. aureus* infection and showed acceptable tissue compatibility in a rabbit femoral model [61]. Cu-bearing stainless steel

implants supported osteogenesis without provoking severe inflammatory responses in a rat model [62]. In another study using copper-containing stainless steel implants, enhanced bone regeneration was observed, promoting both angiogenesis and osteogenesis in a mouse tibial hole model [63]. In a canine model of early peri-implantitis, Ti–Cu dental implants were more effective in inhibiting infection-induced bone resorption compared to pure Ti implants [77] []. In vascular biomedical applications, stent implants manufactured from 316L stainless steel and a cobalt-chromium alloy containing Cu have been shown to markedly reduce vascular smooth muscle cell proliferation and improve arterial blood flow in a rabbit artery model [65]. In contrast, a long-term evaluation of Zn–Cu stents in porcine coronary arteries revealed sustained patency without thrombosis or significant inflammation over a two-year period [66]. More recently, additively manufactured scaffolds containing copper ions have been shown to promote early angiogenesis and initial tissue regeneration in a rat skull bone defect model, further underscoring the potential of copper for enhancing regenerative outcomes [67]. In addition to bulk alloy development, surface modification techniques such as double glow plasma surface alloying (DGPSA) have been successfully used to apply Cu-based coatings with high bonding strength, antibacterial performance, and biocompatibility, further supporting their clinical potential [68]. Collectively, these preclinical *in vivo* studies highlight the potential of copper-containing alloys to enhance antimicrobial protection and tissue regeneration, supporting their future application in biomedical settings.

In our previous study [49], we investigated the composition, structure and electrochemical behavior of Ti–6Al–4V fabricated by annular laser beam (ALB) powder DED-LB process and compared it to the wrought alloy produced by conventional metallurgy. As mentioned in the literature discussed above, the addition of 4 wt% Cu to Ti–6Al–4V provides effective antibacterial activity while maintaining the essential properties of the base alloy. Therefore, in this study, Ti–6Al–4V–4Cu is selected as the starting composition. The work focuses on the investigation of the Ti–6Al–4V–4Cu alloy fabricated by the ALB powder DED-LB process, with a particular emphasis on the influence of the DED build strategies, microstructural characteristics, corrosion behavior, and biocompatibility. Various wall build strategies, including deposition path, ALB deposition power, and ALB initial power, were investigated to identify the strategy that ensures DED-LB process stability and adequate interlayer bonding. Grain morphology was examined using optical microscopy. Microstructural characterization of the alloy was conducted through scanning electron microscopy (SEM), energy-dispersive X-ray spectroscopy (EDS), and X-ray diffraction (XRD). Electrochemical measurements were conducted in a simulated physiological solution to test corrosion properties. Finally, *in vivo* biocompatibility testing of DED-LB fabricated Ti–6Al–4V–4Cu was carried out in an animal model.

2. Materials and methods

2.1. Experimental setup and materials

A powder DED-LB system utilizing an annular laser beam and axially fed powder (Fig. 1) was employed to perform the experiments. The energy source used was an Alta Medium Power continuous fiber laser from nLight, operating at a maximum power of 2650 W and a wavelength of 1080 nm. In the DED-LB process, a ring-shaped ALB intensity distribution with an outer diameter of 3 mm was used [69]. The system utilized a two-channel Oerlikon Metco Twin 150 disc powder feeder, which enabled the simultaneous independent feeding of two powder materials. The required composition of the powder mixture to fabricate Ti–6Al–4V–4Cu alloy is achieved by calibrating the disc powder feeder to deliver 5.76 g/min of Ti–6Al–4V and 0.24 g/min of Cu while maintaining a total mass flow rate of 6 g/min. The powder mixture was fed through the axial powder delivery nozzle into the melt pool. An inert Ar atmosphere with the oxygen content below 0.5 % is maintained in the build chamber, thereby preventing oxidation of the melt. As substrate material, wrought Ti–6Al–4V plates of dimension L × W × D = 90 mm × 15 mm × 3 mm were used, which were clamped on a water-cooled mount maintained at a constant temperature of 19 °C.

To fabricate Ti–6Al–4V–4Cu alloy, nearly spherical plasma-atomized Tekmat Ti–6Al–4V Grade 23 and inert gas-atomized Oerlikon Metco 55 Cu powders were employed, with manufacturer-specified particle size ranges of 45–105 μm and 38–90 μm, respectively. Fig. 2 presents optical microscope images of the powder particles along with particle equivalent diameter distributions for Ti–6Al–4V (Fig. 2a) and Cu (Fig. 2b). As can be observed, both distributions are very similar and exhibit slight positive skewness. The distributions were determined on representative samples of size larger than 100,000 particles by transmission optical microscopy [70].

2.2. DED-LB wall build strategies

To investigate the stability of the powder DED-LB process, which is reflected in the repeatable rectangularity of the walls, a set of walls was fabricated using different build strategies determined by the deposition path (uni- and bi-directional), the ALB deposition power (constant and

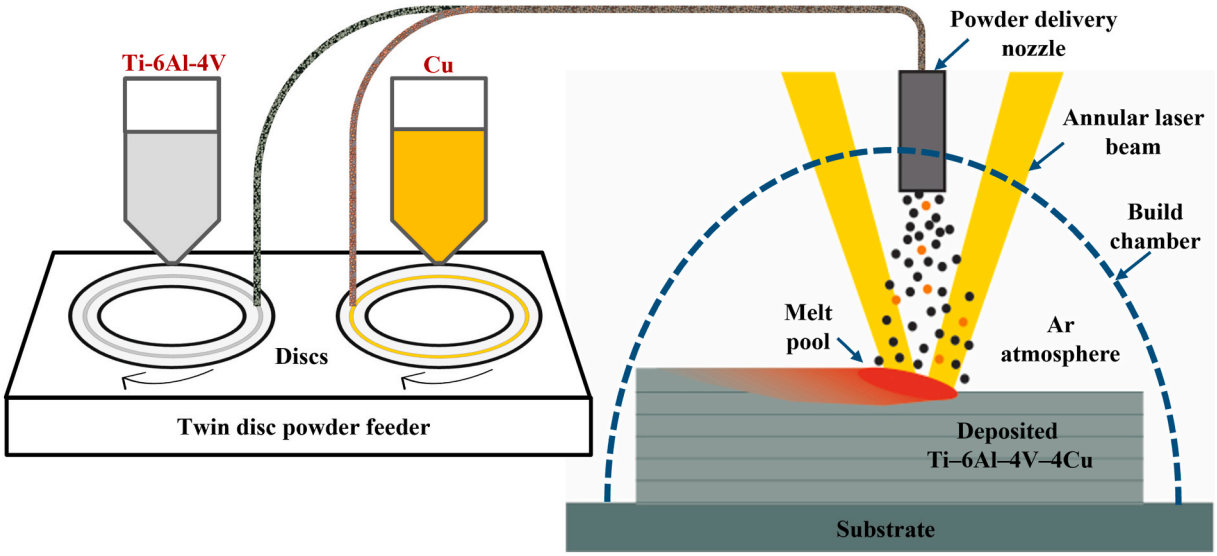

Fig. 1. Experimental setup of the powder DED-LB system.

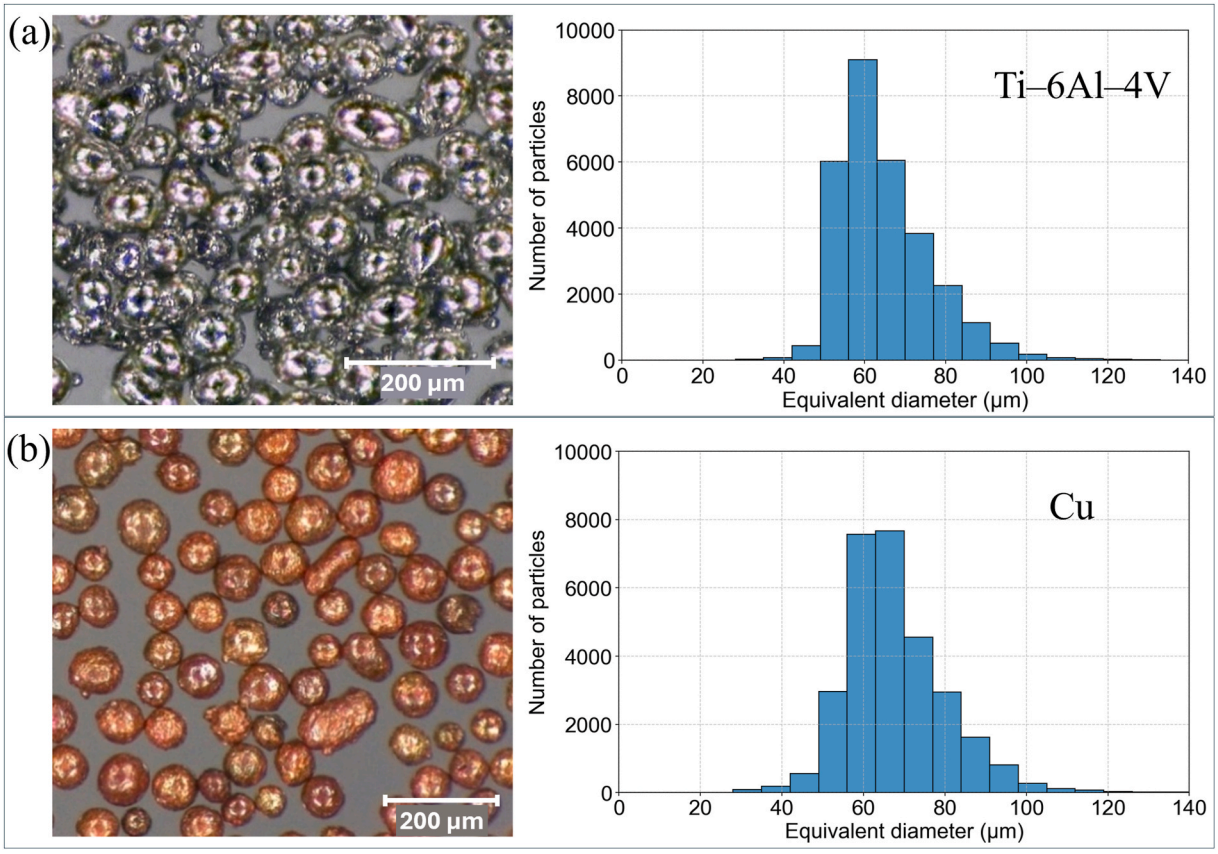

Fig. 2. Optical microscopy images and particle size histograms of the used powders: (a) Ti–6Al–4V, and (b) copper.

reducing) and the ALB initial power P_o, as shown schematically in Fig. 3. In the uni-directional deposition path, the DED-LB process occurs in a single direction along the wall and in the bi-directional deposition path in both directions, as shown schematically in Fig. 4a and b. For deposition path comparison, the effect of time was eliminated by introducing a 5-s dwell time before each layer in the bi-directional deposition path

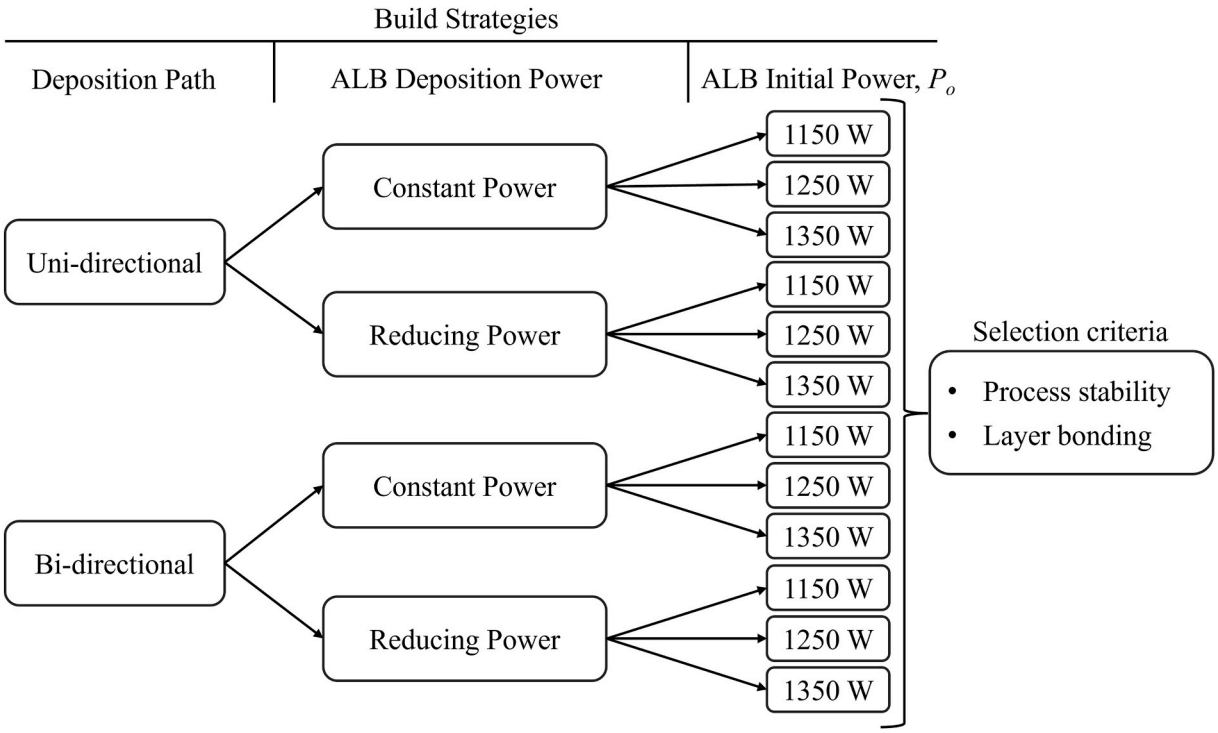

Fig. 3. Scheme of the DED-LB Ti–6Al–4V–4Cu wall build strategies.

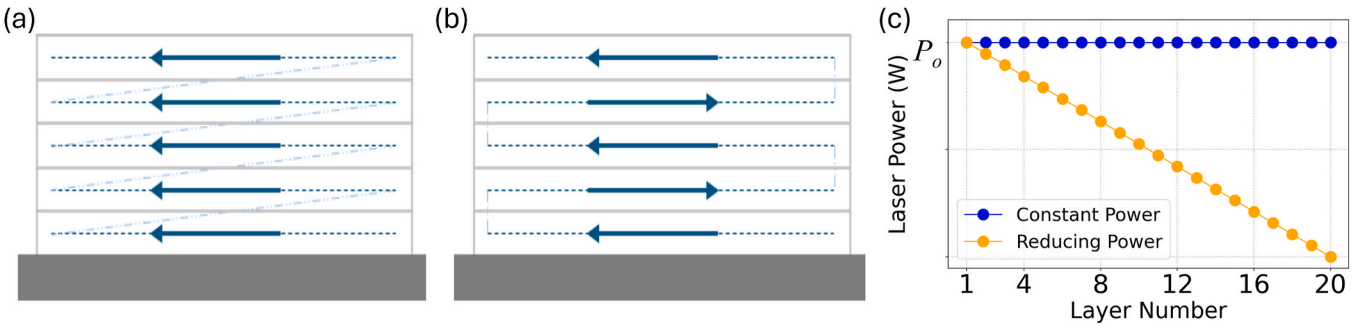

Fig. 4. Schematic presentation of a) uni-directional and b) bi-directional deposition path, c) constant and reducing ALB deposition power.

strategy, thereby equalizing the total deposition time for both deposition path strategies.

The two DED-LB deposition path strategies were performed with either constant or reducing ALB deposition power (10 W per layer) (Fig. 4c), using three ALB initial power P_o values of 1150 W, 1250 W, and 1350 W for the deposition of the first layer. The deposition of 20 layers with a layer height of 1 mm on a wrought Ti–6Al–4V substrate resulted in a wall with a height of 20 mm, a length of 70 mm, and a thickness of 3 mm.

2.3. Materials characterization

To characterize the microstructure, composition and electrochemical properties of the fabricated Ti–6Al–4V–4Cu alloy, discs with a diameter of 15 mm and a thickness of 2 mm were cut from the fabricated walls as shown in Fig. 5.

Before surface analysis, electrochemical measurements and implantation into mice, DED-LB disc samples were metallographically prepared in three mechanical and chemo-mechanical steps: (i) water-grinding using MD Mezzo 220, (ii) polishing using MD Largo + DiaPro, 9 μm and (iii) chemo-mechanical polishing using MD Chem + OP-S (SiO_2, 0.25 μm + 10 % v/v H_2O_2) [71]. All polishing cloths and lubricants were distributed by Struers (Ballerup, Denmark).

For the analysis of the microstructure, the surface was etched for 40 s using Kroll's solution, which consisted of 100 mL water, 4 mL nitric acid (HNO_3), and 2 mL hydrofluoric acid (HF). The etched surface was examined by optical microscopy (Keyence VHX-6000).

The XRD characterization was performed on a 1 cm^2 sample area on an X-ray powder diffractometer (PANalytical X'Pert PRO) with Cu Kα radiation in the range from 30° to 90° 2Θ with a step of 0.0033° 2Θ and 100 s per step. The qualitative and quantitative analyses were done by the X'Pert HighScore 4.9 program (Malvern Analytical B.V., Almelo, The Netherlands) with an in-built Rietveld refinement program (15 parameters were refined - scale factors and unit cell parameters for each phase, as well as background and sample displacement parameters).

SEM analysis was conducted using a FEI Helios 650 Nanolab instrument, operating at a beam acceleration voltage of 10 kV. Imaging was performed using a circular back-scattered (CBS) detector for back-scattered electrons (BSE) to obtain compositional information, as they provided a contrast between areas with different chemical compositions. In addition to SEM analysis, EDS was conducted using an Oxford Instruments AZtec system with an X-max SDD (50 mm^2) detector at 10 kV. The volume fractions of the individual phases were quantified using ImageJ (U. S. National Institutes of Health) based on contrast differences. The process involved cropping the images to exclude irrelevant regions, converting them to 8-bit grayscale, and applying fixed threshold values to distinguish phases by their grayscale intensities.

Electrochemical measurements were performed in a custom-built three-electrode cell, constructed from polymethylmethacrylate with a volume of 250 mL. The cell was equipped with a thermostatic jacket to maintain a constant temperature of 37 ± 0.1 °C throughout the experiments. The DED-LB sample, with an exposed surface area of 1 cm^2, was used as the working electrode placed at the bottom of the cell using a holder. A saturated silver/silver chloride (Ag/AgCl) electrode, with a potential of 0.197 V relative to the standard hydrogen electrode, was employed as the reference electrode. In the text, potentials are given relative to the Ag/AgCl scale. The counter electrode was a graphite rod with a diameter of 5 mm. All electrochemical testing was conducted using an Autolab PGSTAT M204 multipotentiostat/galvanostat (Metrohm Autolab, Nova software version 2.1.6, Utrecht, The Netherlands).

Electrochemical measurements were conducted in Hanks' balanced salt solution (HBSS) with the following composition: 8 g/L sodium chloride (NaCl), 0.4 g/L potassium chloride (KCl), 0.19 g/L calcium dichloride dihydrate ($CaCl_2 \times 2H_2O$), 0.06 g/L magnesium sulfate ($MgSO_4 \times 7H_2O$), 0.40 g/L magnesium chloride hexahydrate ($MgCl_2 \times 6H_2O$), 0.35 g/L sodium hydrogen carbonate ($NaHCO_3$), 1 g/L glucose

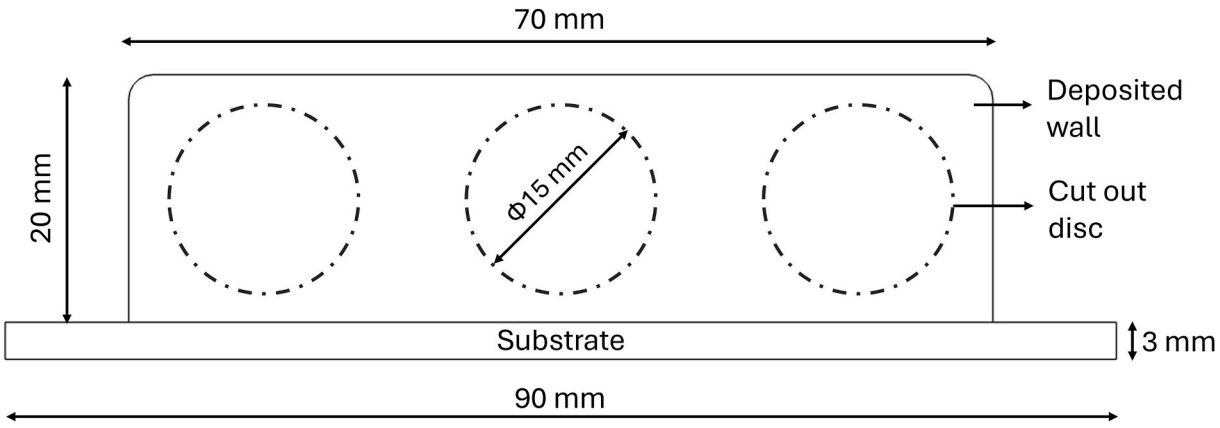

Fig. 5. The geometry of the wall and the location of the cut-out discs.

(D-Glucose), 0.25 g/L potassium dihydrogen phosphate ($KH_2PO_4 \times H_2O$), 0.06 g/L disodium hydrogen phosphate ($Na_2HPO_4 \times 2H_2O$); pH ~ 7.2–7.4 [49]. All chemicals were analytically pure and distributed by Sigma Aldrich (Steinham, Germany).

The sample was stabilized at open-circuit potential (OCP) for 1.5 h, followed by the recording of the potentiodynamic polarization (PDP) curve at a scan rate of 1 mV/s. The scan started from −0.15 V vs. OCP and progressed to 4.0 V. Electrochemical parameters, including corrosion potential (E_{corr}) and corrosion current density (j_{corr}), were extracted from the PDP curves using Nova 2.1.6 software. Representative measurements were selected for graphical presentation, and mean values with standard deviations of electrochemical parameters were reported in Table 2.

2.4. *In vivo* biocompatibility evaluation in a mouse subcutaneous implantation model

To evaluate the biocompatibility of the Ti–6Al–4V–4Cu alloy, an *in vivo* study was performed using a subcutaneous disc implantation model in 10-week-old female C57BL/6JOlaHsd mice. For implantation, small discs with a diameter of 5 mm and a thickness of 1 mm were cut from the wall. Four groups were included: a sham-operated control group (surgery without implant) (n = 14), a Ti–6Al–4V alloy group (n = 18), a Ti–6Al–4V–4Cu (4 % Cu) alloy group (n = 18), and a baseline group that did not undergo surgery (n = 15). Sterile disc-shaped implants (5 mm diameter, 1 mm thickness) were inserted subcutaneously between the scapulae using a minimally invasive surgical approach [72] under ketamine/xylazine anesthesia. Animals were monitored daily for wound healing, general health, and signs of discomfort using the Mouse Grimace Scale (MGS) [73]. Blood and tissues were analyzed for local and systemic effects at Day 7 (acute phase) and Day 56 (chronic phase) post-implantation. Group sizes were as follows: Ti–6Al–4V group (n = 9 per timepoint), Ti–6Al–4V–4Cu group (n = 9 per timepoint), sham-operated group (n = 8 at Day 7, n = 6 at Day 56), and baseline (no-treatment) group (n = 7 at Day 7, n = 8 at Day 56). Blood was first collected from the tip of the tail for hematological analysis (VetScan HM5, 24 parameters, Zoetis, USA) and then from neck vein vessels following decapitation. For biochemistry profiling (VetScan Comprehensive Diagnostic Profile, 14 parameters) fresh serum was used whereas serum was frozen for a subsequent measurements of metal ions (see section 2.4.1).

For histological analyses, three tissue types were collected from each animal: connective tissue surrounding the implant, tissue directly adjacent to the implant, and skin. Samples were fixed in 4 % formalin, embedded in paraffin, sectioned, and stained with hematoxylin and eosin (H&E). Slides were examined under a light microscope (Nikon Eclipse 80i), and representative images were captured with a digital camera (Nikon DS-Fi2).

All procedures involving animals were conducted in accordance with Directive 2010/63/EU, the Slovenian Animal Protection Act, and approved by the Administration of the Republic of Slovenia for Food Safety, Veterinary and Plant Protection (approval number: U34401-23/2023/8).

2.4.1. Measurements of metal ions in mouse serum

Elemental concentrations of aluminum (Al), titanium (Ti), vanadium (V), and copper (Cu) were determined employing inductively coupled plasma mass spectrometry (ICP-MS). An Agilent Technologies 7700x ICP-MS (Tokyo, Japan) instrument was used. The ICP-MS operating parameters were optimized for plasma robustness and adequate sensitivity. For the removal of polyatomic interferences, collision mode was applied, using helium as the collision gas. The ICP-MS operating parameters are provided in supplementary material, Table S1. A Mettler Toledo MS104 analytical balance (Zürich, Switzerland) was used for weighing.

Ultrapure water (18.2 MΩ cm) from a Direct-Q 5 Ultrapure Water System (Millipore, Watertown, MA, USA) was used to prepare calibration standards and samples. Nitric acid (HNO_3) s.p. purchased from Carlo Erba (Milan, Italy) was used for standard preparation. Merck ICP multi-element standard solution VI Certipur® from Merck (Darmstadt, Germany) was used to prepare calibration standards. The accuracy of the determination of total element concentrations in serum was verified by analyzing the certified reference material, Trace Elements in Serum L-2, obtained from SERO AS (Billingstad, Norway), which is certified for Al and Cu concentrations. Good agreement was obtained between the determined elemental concentrations (within ±5 %) and the certified values, confirming the accurate determination of total concentrations in serum by ICP-MS. These data are provided in Supplementary Material, Table S2. Since Ti and V concentrations are not certified in the Serum L-2 reference material, a spike recovery test was applied. For this purpose, Serum L-2 was spiked with Ti and V at a concentration of 10 ng/mL. The recoveries obtained were within ±5 %.

Before analysis, all serum samples were thawed and equilibrated to room temperature. A 100 μL aliquot was transferred into a plastic tube, and the content was weighed using a precise analytical balance. Before the analysis, the sample was diluted 10 times with Milli-Q water. The amount of water was also measured by weighing. Elemental concentrations were determined by ICP-MS using an external calibration mode. All samples were measured in duplicate.

3. Results and discussion

3.1. Material fabrication and test sample preparation

Fig. 6 shows examples of the side view of the Ti–6Al–4V–4Cu walls fabricated using different build strategies, at ALB initial power of P_o = 1250 W. In the case of the uni-directional deposition path (Fig. 6a and b), the images highlight instability in the form of a slight waviness and asymmetry in the rectangular shape due to the one-sided DED run-out. In contrast, a more symmetrical rectangular shape of the wall was achieved with a bi-directional deposition path (Fig. 6c and d), indicating a higher process stability with this approach. With the reducing power (Fig. 6d), the rectangularity of the wall was further improved.

Based on process stability criteria and related wall shape (Fig. 3), the bi-directional deposition path with decreasing power was selected as the suitable build strategy. The appropriate ALB initial power P_o was then selected based on optical microscopy images of the layer bonding at different values of ALB initial power, P_o = 1150 W, 1250 W, and 1350 W, shown in Fig. 7. In the case P_o = 1150 W (Fig. 7a), a lack of fusion resulted in partially melted particles (indicated by arrows) between the successive layers, demarcated by a dashed line. In the cases P_o = 1250 W and 1350 W (Fig. 7b and c), the deposited layers were well bonded from bottom to top, leading to the selection of the ALB initial power P_o = 1250 W.

Considering the qualitatively presented impact of the build strategy on process stability related to the rectangularity of the wall and interlayer bonding properties, the bi-directional deposition path with reducing power and ALB initial power P_o = 1250 W was selected as the optimal build strategy for further characterization.

3.2. Materials characterization

3.2.1. Microstructure and chemical composition by SEM/EDS analysis

Generally, the build strategy affects the shape and orientation of the grains [74]. In agreement with previous studies on microstructure [33], the addition of Cu in Ti–6Al–4V resulted in the formation of equiaxed grains (highlighted in Fig. 7b) across all Ti–6Al–4V–4Cu fabricated samples, regardless of the build strategy.

The results for the DED-LB Ti–6Al–4V sample prepared without Cu addition were given in our previous study [49,71]. The Ti–6Al–4V predominantly consists of the Al-rich α phase, intersected with a V-rich β phase. The chemical composition was comparable to the metallurgically

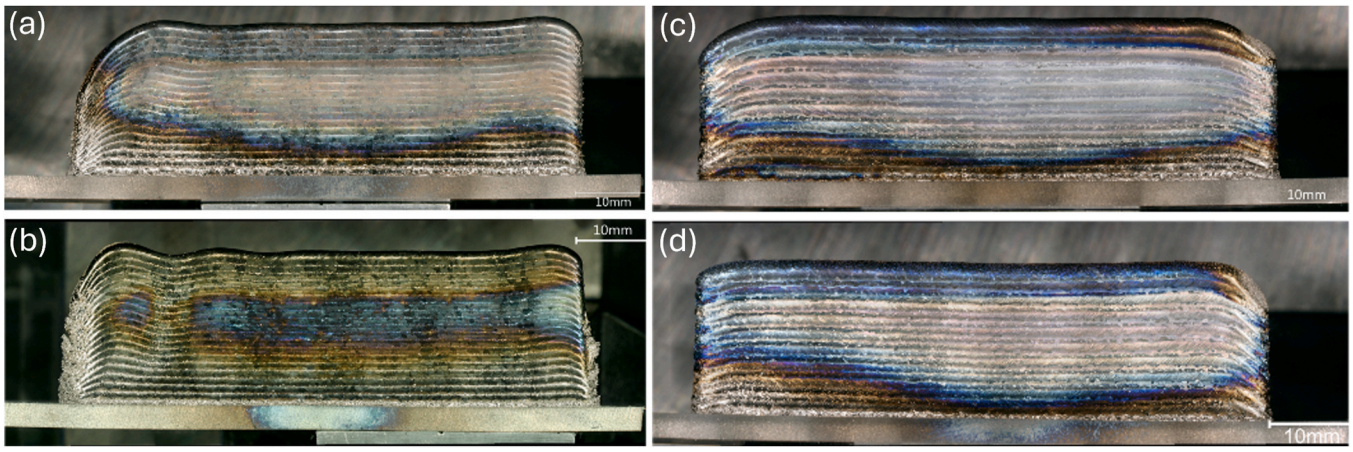

Fig. 6. Influence of DED-LB build strategy on the process stability and related shape of the fabricated Ti–6Al–4V–4Cu wall: (a) uni-directional path and constant power, (b) uni-directional path and reducing power, (c) bi-directional path and constant power, (d) bi-directional path and reducing power.

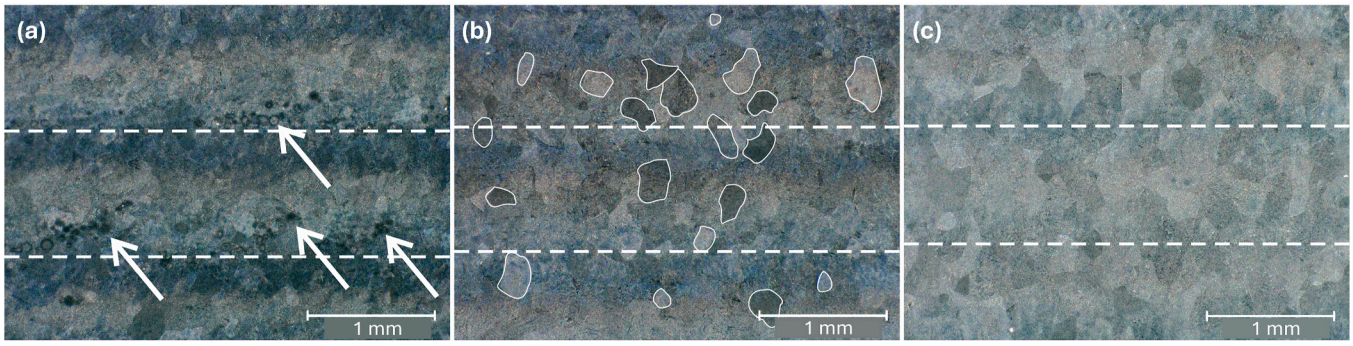

Fig. 7. Optical microscopy images of layer bonding at different ALB initial power P_o values: (a) 1150 W, (b) 1250 W, (c) 1350 W. All samples were fabricated with a bi-directional path and reducing ALB power.

produced alloy, i.e., 6.0 wt% Al, 4.2 wt% V and the rest Ti. The microstructure and chemical composition of the DED-LB Ti–6Al–4V–4Cu sample prepared with the selected build strategy are presented by the BSE SEM image in Fig. 8. The colors in BSE images differ in composition related to the atomic number; the higher the atomic number (corresponding to the heavier the element), the brighter the material appears in the image. The Al-rich α matrix phase is dark grey and occupies most of the sample surface, and light grey, V-rich β phase spreads longitudinally along the α phase. Compared to the Ti–6Al–4V sample [49], however, the addition of copper causes the formation of an additional phase represented by the bright particles along the edge of the β phase. The accompanying EDS analysis, performed over the entire area of the surface captured by SEM analysis, revealed a composition of 5.3 wt% Al, 3.3 wt% V, 3.9 wt% Cu and the rest Ti (Table 1), thus confirming the successful deposition of the Ti–6Al–4V–4Cu alloy using DED-LB.

Furthermore, the EDS point analysis was conducted at various locations (phases) on the sample's surface for closer inspection (Fig. 8 and Table 1). When examining the prevailing dark grey, Al-rich α phase (location 1), the Cu content is approximately 2 wt%, which is smaller than that determined for the whole image area (approximately 4 wt%). In the β phase (light grey phase, location 2), the Cu content was around 5 wt%. The Cu content was the highest at 15 wt% in the Cu-rich phase (location 3). The results show that when performing EDS analysis over a larger area, the average composition obtained is insufficiently sensitive to account for lateral differences. However, point EDS analysis clearly showed that the concentration of Cu is the highest in the bright particles formed along the edges of the β phase. This new phase in the alloy corresponds to Ti_2Cu, as evidenced by the XRD analysis (see below).

The phase fractions of the three constituent phases were contrasted and quantified to show volume fractions of individual phases (Fig. 8b–d. The α phase accounts for approximately 85 %, the β phase for 12 %, and the Ti_2Cu phase for 3 % (Fig. 8e). The Ti_2Cu particles are always located along the edges of the β phase. Determining the average size of the Ti_2Cu particles is challenging using image analysis due to the nanometric size of the particles. Judging from the SEM images, the particle size ranges from 50 nm to approximately 200 nm.

3.2.2. XRD phase analysis

The XRD diffraction spectra of the Ti–6Al–4V–4Cu sample fabricated with the selected build strategy are presented in Fig. 9. The X-ray diffraction pattern of the DED-LB Ti–6Al–4V sample was described in our previous study [49] and is given here for comparison. Briefly, the prominent XRD peaks aligned with α-Ti (hcp) phase (ICDD PDF#04-023-7232) were noted with the prominent peaks at 35.3°, 38.5°, 40.4°, 53.2°, 63.4°, and 76.7° (2Θ) (crystallographic orientations are denoted in the figure). The spectrum of DED-LB samples is regarded as the martensite α′-Ti phase [49]. In addition, peaks related to the β-Ti phase were noted. The position of the peaks is aligned with the β phase (ICDD PDF#01-081-9813), with the prominent peaks at 39.4°, 56.9°, and 71.4° (2Θ). These peaks are denoted as β′-Ti since they are positioned slightly differently from the β-Ti of the wrought alloy, presumably due to the different thermal histories of the two processes.

The prominent difference of the XRD spectrum of Ti–6Al–4V–4Cu compared to non-Cu containing alloys is the Ti_2Cu peaks at 39.5°, 43.5°, and 77.1° (2Θ). There are some overlaps of the peaks, i.e., the peak at 39.5° (2Θ) related to (103) Ti_2Cu is close to (110) β′-Ti, but the former peak in the Cu-containing alloy is much more intense.

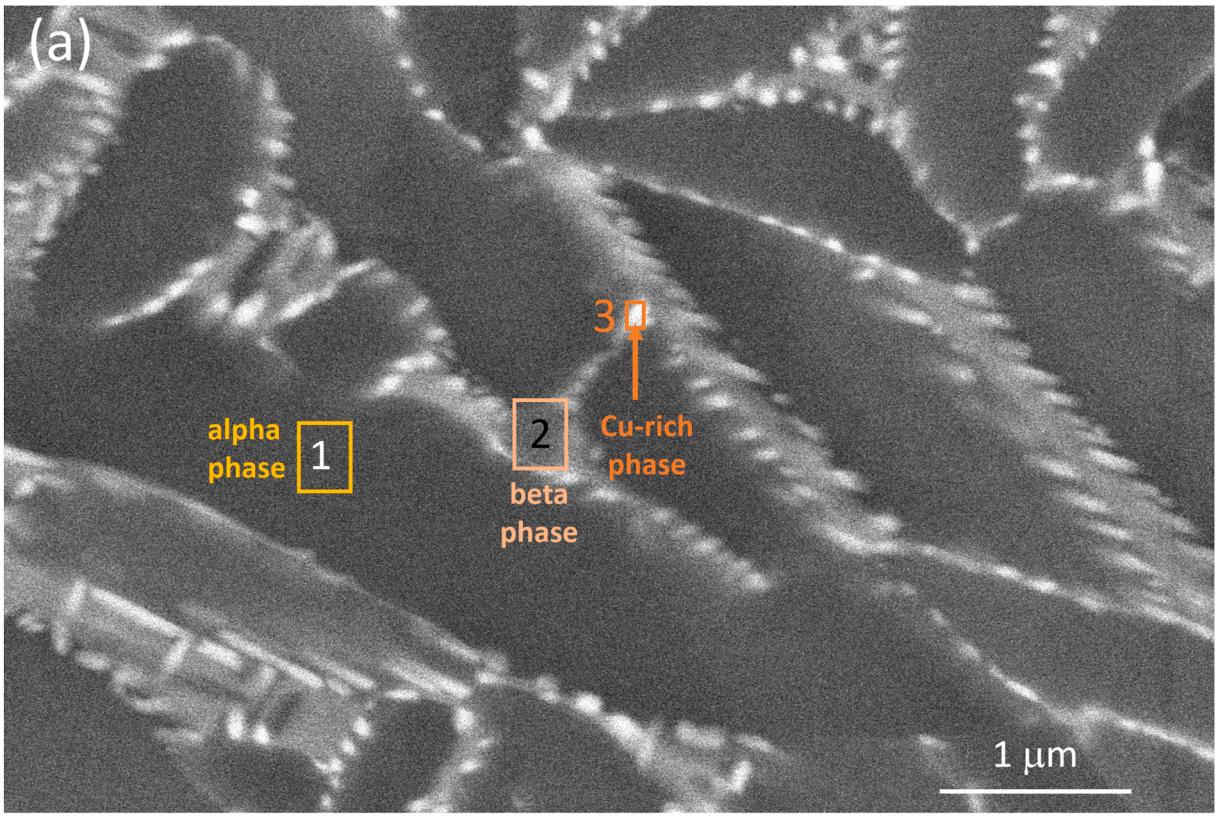

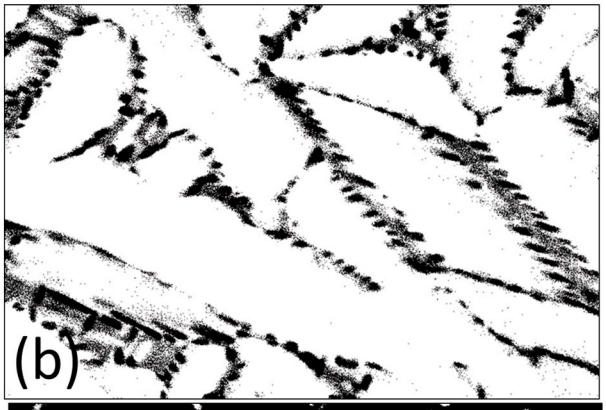

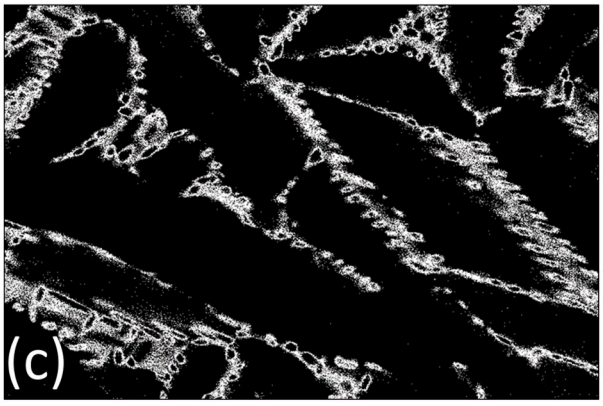

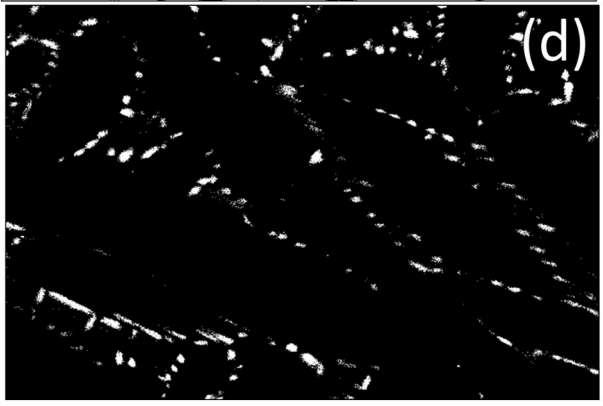

(e)

phase	Volume fraction
(b) α	84.9
(c) β	12.3
(d) Ti_2Cu	2.8

Fig. 8. (a) Back-scattered SEM image of surface morphology for DED-LB manufactured Ti–6Al–4V–4Cu sample fabricated with the selected build strategy. The image was recorded at a magnification of 20,000×. EDS compositional analysis conducted at the numbered sites is presented in Table 1. (b–c) Contrasted individual α, β and Ti_2Cu phases and (e) their volume fractions quantified using the ImageJ programme.

Table 1
Composition determined by EDS analysis conducted at various spots of DED-LB Ti–6Al–4V–4Cu sample (Fig. 8). Please note that standardless EDS is a semi-quantitative analysis. For Ti as a major element, the composition is rounded to 1 wt %, as well as for O as a light element.

Site	Composition/wt.%				
	Ti	Al	V	Cu	O
whole image	84	5.3	3.3	3.9	2
1	85	5.9	2.9	2.3	3
2	84	5.5	3.5	2.4	3
3	78	4.5	11.1	5.3	–
4	73	4.4	3.7	15.6	2

Table 2
Electrochemical data for DED-LB Ti–6Al–4V and Ti–6Al–4V–4Cu samples obtained from potentiodynamic measurements in HBSS are presented in Fig. 10. OCP - open circuit potential, E_{corr} - corrosion potential, and j_{corr} - corrosion current density.

Sample	OCP [V]	E_{corr} [V]	j_{corr} [nA cm^{-2}]
Ti–6Al–4V	−0.360 ± 0.061	−0.345 ± 0.088	11.6 ± 3.63
Ti–6Al–4V–4Cu	−0.326 ± 0.126	−0.371 ± 0.119	16.7 ± 7.92

3.2.3. *Electrochemical measurements of DED-LB Ti–6Al–4V and Ti–6Al–4V–4Cu samples*

The electrochemical properties of both DED-LB Ti–6Al–4V and Ti–6Al–4V–4Cu samples were considered. Potentiodynamic polarization (PDP) curves recorded in Hanks' balanced salt solution (HBSS) (pH = 7.2–7.4, 37 °C) for both samples are presented in Fig. 10. Typical electrochemical parameters of open circuit potential, OCP, corrosion potential, E_{corr}, and corrosion current density, j_{corr}, deduced from the PDP curves are presented in Table 2.

Upon immersion in HBSS, both samples show very similar OCP, between −0.10 and −0.13 V, the latter being slightly more negative for Ti–6Al–4V–4Cu (Fig. S1). During the first hour of immersion, OCP shifted more negatively and then remained approximately constant until the end of the immersion. The mean values of OCP were −0.360 ± 0.061 V and −0.326 ± 0.126 V for Ti–6Al–4V and Ti–6Al–4V–4Cu samples, respectively.

After starting the potentiodynamic scan −0.15 V relative to stabilized OCP (Fig. 8), the current density progressively decreased in the cathodic range down to the E_{corr} and then increased again in the anodic range. When analyzing typical electrochemical parameters in the narrow range around the corrosion potential, it is observed that the materials exhibit similar behavior (Table 2). The values of E_{corr} are −0.345 ± 0.088 V and −0.371 ± 0.119 V for DED-LB Ti–6Al–4V and Ti–6Al–4V–4Cu, respectively. Similarly, j_{corr} values are 11.6 ± 3.63 nA/cm^2 and 16.7 ± 7.92 nA/cm^2; thus, E_{corr} and j_{corr} were slightly more negative (for 25 mV) and marginally higher (for 5 nA/cm^2) for the sample containing copper.

However, in the anodic region, the differences between the two samples became more apparent. The rise in current density continued from E_{corr} up to approximately 0 V. In this potential range, the current density rose slightly steeper for the sample without Cu, and also the onset potential of the current density plateau was somewhat more negative, i.e., 0.06 V compared to 0.18 V for Ti–6Al–4V–4Cu. Although the effect is minor, it indicates that the addition of Cu slightly affects the kinetics of self-passivation. At the first plateau, the current density remained at $4{\cdot}10^{-5}$ A cm^{-2} despite further increase in electrode potential. This passivation effect is related to the progressive coverage of the surface by a TiO_2 layer, preventing further metal dissolution [49, 71]. For the Ti–6Al–4V, this plateau extends to 2.65 V. At more positive potentials, the current density increased and a second current density plateau was established at $6{\cdot}10^{-3}$ A cm^{-2}, as described previously [49, 71].

For the Ti–6Al–4V–4Cu, however, the first current density plateau

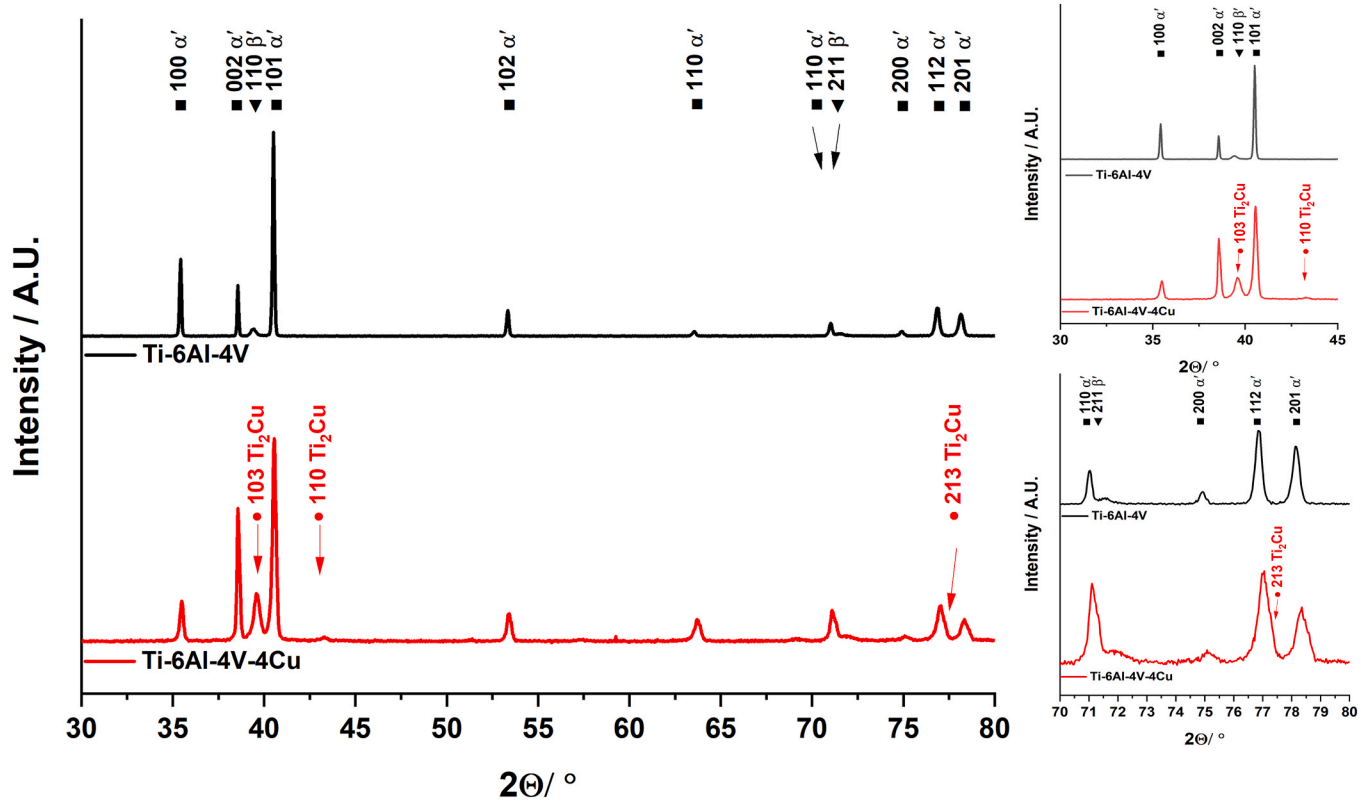

Fig. 9. The XRD diffraction (normalised) patterns of the DED-LB Ti–6Al–4V–4Cu sample recorded in the range 30–80° (2Θ). The spectrum for the DED-LB Ti–6Al–4V sample, fabricated with the same build strategy, is given for comparison. Enlarged spectra in the 30–45° and 70–80° (2Θ) range are shown in the right panel.

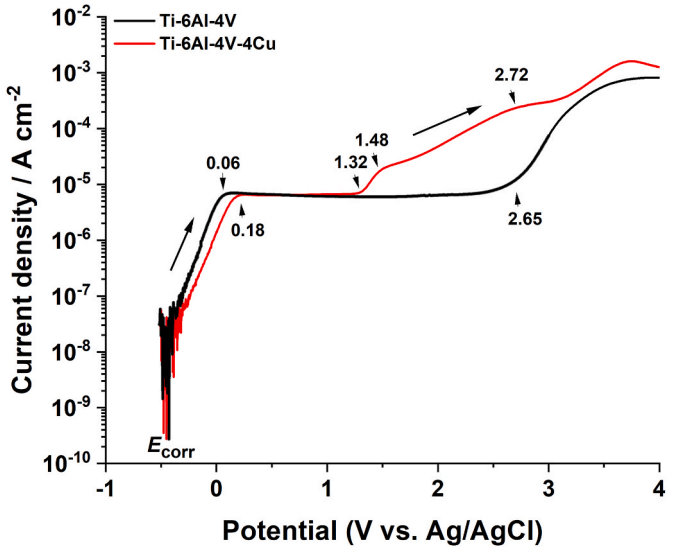

Fig. 10. Potentiodynamic polarization curves of DED-LB manufactured Ti–6Al–4V and Ti–6Al–4V–4Cu samples after 1.5 h of immersion in Hanks balanced salt solution (HBSS) (pH = 7.4, 37 °C). Curves were recorded using a scan rate of 1 mV/s. Both samples were printed using the selected build strategy. Electrochemical parameters are presented in Table 2.

extends only to 1.32 V. At more positive potentials, a new feature appears in the form of two not well-resolved current peaks at 1.48 V and 2.72 V. The second current density plateau was reached at somewhat higher current densities than for the Ti–6Al–4V. The features related to the current density increase between 1.3 V and 3 V can be attributed to the presence of copper in the material. Copper is less corrosion-resistant than Ti alloy in the simulated physiological medium, which contains chloride ions. These ions facilitate the dissolution of copper, which then presumably forms a Cu–Ti-rich layer at the surface.

Based on the materials characterization of the Ti–6Al–4V–4Cu alloy, it can be summarized that the alloy exhibits a lamellar structure with α phase containing predominantly Ti and Al, β phase containing Ti, Al, V and Cu and β phase rich in Cu. In terms of electrochemical corrosion characteristics, the PDP curves reflect the passivation capability of both alloys in HBSS. They behave similarly in the range around OCP, but in the anodic range, their behavior differs, with the alloy containing copper showing the formation of a new current peak, presumably related to the formation of a Cu–Ti-containing surface layer.

When comparing the results obtained in this study with the literature data, several differences are observed. PDP curves were reported for Ti–*x*Cu [27,51,52] and Ti–6Al–4V–*x*Cu alloys [20,53–55]. The curves were measured in 3.5 wt% at room temperature [50,53], 0.9 wt% at 37 °C [20,54], simulated body fluid at 37 °C [55], HBSS at 37 °C [51, 52]. Except in Ref. [27], all these samples were prepared by the PBF-LB method. The reported results on the characteristics of the PDP curves largely differ. In several studies, a decrease in current density has been reported with the addition of copper [20,50,51,53]. The content of Cu seems to have only a minor effect on the shape of the PDP curve [20,51]. In another study, the formation of an additional peak was reported for Ti–6Al–4V–*x*Cu alloys with higher Cu contents, i.e., 8 and 10 wt% [55]. In some studies, no comparable measurements were provided for the alloy containing no Cu, making it impossible to make a comparison [52, 54]. Based on the presented literature findings, it appears challenging to directly compare the results obtained from various methods, as well as those from the same type of AM method.

3.3. *In vivo* biocompatibility assessment of Ti–6Al–4V–4Cu implants

The *in vivo* biocompatibility of the Ti–6Al–4V–4Cu alloy produced by additive manufacturing was evaluated using a mouse subcutaneous disc implantation model, focusing on general health, systemic toxicity, and local histological responses (Fig. 11).

The general health and well-being of the mice were monitored throughout the study using daily visual observations, evaluations with the Mouse Grimace Scale (MGS), and measurement of feed intake, water intake, and body weight (Fig. S2). No signs of distress, abnormal behavior, or significant changes in MGS scores were observed at any time point after implantation. Feed intake, water intake, as well as body weight, remained comparable between the Ti–6Al–4V–4Cu alloy, Ti–6Al–4V alloy, and sham-operated control groups on both Day 7 and Day 56.

Systemic hematological responses were assessed by analyzing white blood cell counts, red blood cell counts, hemoglobin levels, and platelet counts on both Day 7 (Fig. 12) and Day 56 (Fig. S3). No significant differences were detected among the Ti–6Al–4V–4Cu, Ti–6Al–4V, sham-operated and untreated control groups at either time point.

Metabolic profiling was performed using the VetScan Comprehensive Diagnostic Profile to assess liver function, kidney function, glucose metabolism, and electrolyte balance. A panel of 14 biochemical parameters was analyzed on both Day 7 (Fig. 13) and Day 56 (Fig. S4). No significant differences were observed among the experimental groups for any of the measured parameters.

Histological analysis showed that all implants were surrounded by a loose connective tissue capsule containing macrophages, fibroblasts, granulocytes, and scattered collagen fibers, with no evidence of granulomatous inflammation. Skeletal muscle fibers and both brown and white adipose tissue were observed in tissue adjacent to the implants, indicating integration with the surrounding soft tissues (Fig. 14). Similar patterns were observed in sham-operated animals (Fig. S5). Skin samples exhibited normal epidermis, a dermis with hair follicles, and subcutaneous adipose tissue in all groups (Fig. 14). Macrophages with dusty black cytoplasm—suggestive of phagocytic activity—were observed in both implant groups, with no apparent differences in their density (Fig. 15). Occasional skin sections from animals across all experimental groups exhibited localized granulocyte infiltration, likely due to self-inflicted scratching. As these findings were restricted to the skin and unrelated to the implant site, they are not indicative of an implant-specific inflammatory response (Fig. S6).

3.3.1. *Measurements of metal ions in serum*

The concentrations of metal ions measured by ICP-MS on Day 7 and Day 56 for baseline, sham, Ti–6Al–4V, and Ti–6Al–4V–4Cu groups are given in Fig. 16. The detailed results are given in Table S3. Among all the metal ions, copper had the highest concentration in the mouse blood before the operation (baseline), about 449 ng/g. The concentrations of Al, V, and Ti were 30–60 times smaller. At Days 7 and 56, no significant differences were observed, indicating that the concentrations remained at a similar level and that the implantation of either disc type did not promote increased metal release into the blood.

The *in vivo* evaluation confirmed that Ti–6Al–4V–4Cu alloy implants exhibited excellent biocompatibility, with no evidence of systemic toxicity, metabolic disturbances, or local inflammatory responses. Across a range of physiological readouts - including feed and water intake, body weight, behavioral indicators, hematological, metabolic parameters, and histological findings - no significant differences were detected between the Ti–6Al–4V–4Cu alloy group and either the Ti–6Al–4V or control groups at either Day 7 or Day 56. These results indicate that the introduction of 4 wt% copper did not elicit detectable systemic toxicity or adverse local effects in this murine subcutaneous model. The stable physiological and behavioral outcomes observed throughout the whole 56-day observation period further support the alloy's safety profile. Some previous studies examining Cu-containing metal implants *in vivo* have reported similar findings across different species and anatomical models. For example, Ti–Cu implants in rabbit femur [61], Cu-stainless steel discs in rats [62], and Ti–Cu dental

Fig. 11. Surgical implantation and post-operative outcome of Ti–6Al–4V–4Cu alloy discs. (a) Sterile disc-shaped implants (5 mm × 1 mm) were inserted subcutaneously between the scapulae of anaesthetised mice via a minimally invasive approach. (b) By Day 10, the wound showed full closure, good healing, and no signs of inflammation or distress.

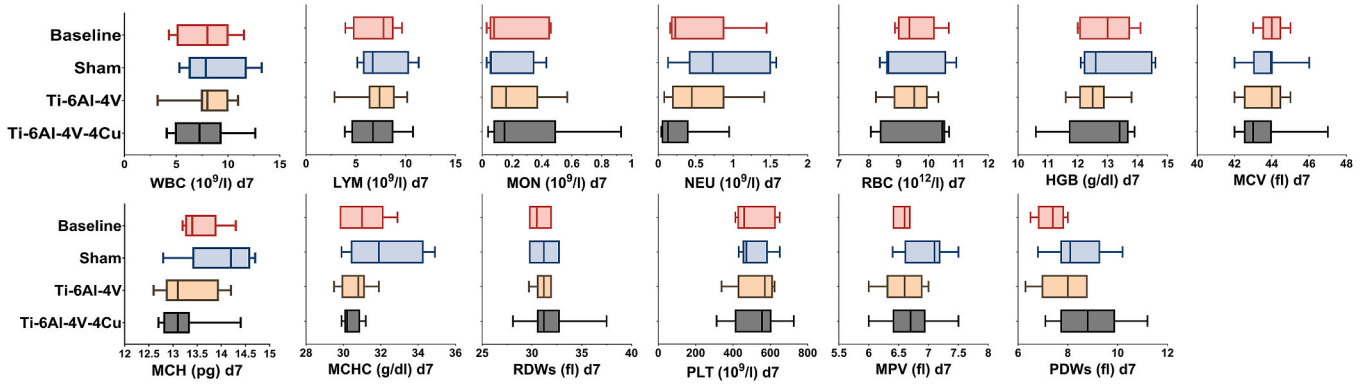

Fig. 12. Hematological parameters at Day 7 after implantation of Ti–6Al–4V–4Cu alloy discs. A panel of 24 parameters was analyzed to assess systemic effects, and no group differences were found at Day 7. Boxplots display medians and interquartile ranges; statistical analysis was performed using one-way ANOVA ($\alpha = 0.01$). Abbreviations: WBC, white blood cell count; LYM, lymphocytes; MON, monocytes; NEU, neutrophils; RBC, red blood cell count; HGB, haemoglobin; MCV, mean corpuscular volume; MCH, mean corpuscular haemoglobin; MCHC, mean corpuscular haemoglobin concentration; RDWs, red cell distribution width; PLT, platelet count; MPV, mean platelet volume; PDWs, platelet distribution width.

implants in beagle dogs [9] have shown no evidence of systemic toxicity, while promoting tissue integration or osteogenesis. While differences in implantation site, alloy composition, and animal species preclude direct comparison, the overall findings are consistent with a favorable safety profile for biomedical Cu-containing alloys.

Additionally, ICP-MS analysis of blood samples showed no elevation in systemic metal ion levels following implantation—copper concentrations remained stable, and aluminum, vanadium, and titanium levels stayed 30–60 times lower than baseline copper values. This observation aligns with the findings of Sengodan and Doddihithlu (2020), who reported that serum titanium levels remained within normal limits, with no signs of systemic toxicity in patients with orthopedic implants [75]. Similarly, Kram et al. [76] (2022) demonstrated that serum copper levels remained within the non-toxic range (<1.69 mg/L) following implantation of copper-containing urological devices. Together, these results not only confirm the systemic biocompatibility of Cu-containing alloys but also highlight the absence of copper leaching into circulation, supporting their safe long-term use in biomedical applications.

4. Conclusions

This study demonstrates the successful additive manufacturing of Ti–6Al–4V–4Cu alloy using an axial powder DED-LB process with an annular laser beam. The optimal DED-LB build strategies were considered in relation to process stability, specifically in terms of wall shape and interlayer bonding properties. Using the ring laser beam intensity distribution, the bi-directional deposition path with reducing ALB deposition power and an ALB initial power of $P_o = 1250$ W was selected as the optimal build strategy. Microstructural analysis of the fabricated Ti–6Al–4V–4Cu alloy confirmed a homogeneous distribution of α, β, and

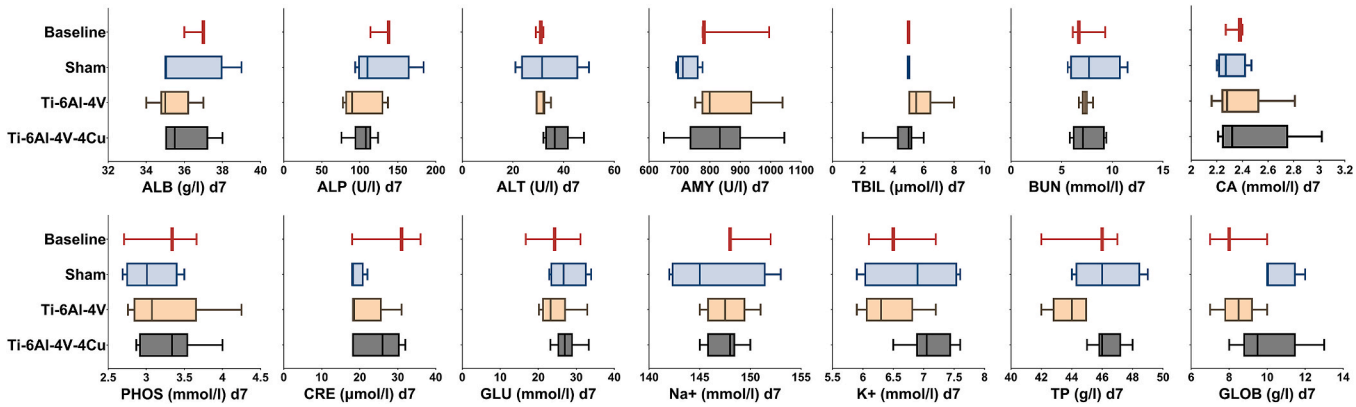

Fig. 13. Metabolic parameters at Day 7 following implantation of Ti–6Al–4V–4Cu alloy discs. A panel of 14 metabolic parameters, assaying liver, kidney, glucose, and electrolytes at Day 7. No significant differences were found among groups. Boxplots display medians and interquartile ranges; statistical analysis was performed using one-way ANOVA ($\alpha = 0.01$). Abbreviations: ALB, albumin; ALP, alkaline phosphatase; ALT, alanine aminotransferase; AMY, amylase; TBIL, total bilirubin; BUN, blood urea nitrogen; CA, calcium; PHOS, phosphorus; CRE, creatinine; GLU, glucose; Na^+, sodium; K^+, potassium; TP, total protein; GLOB, globulin.

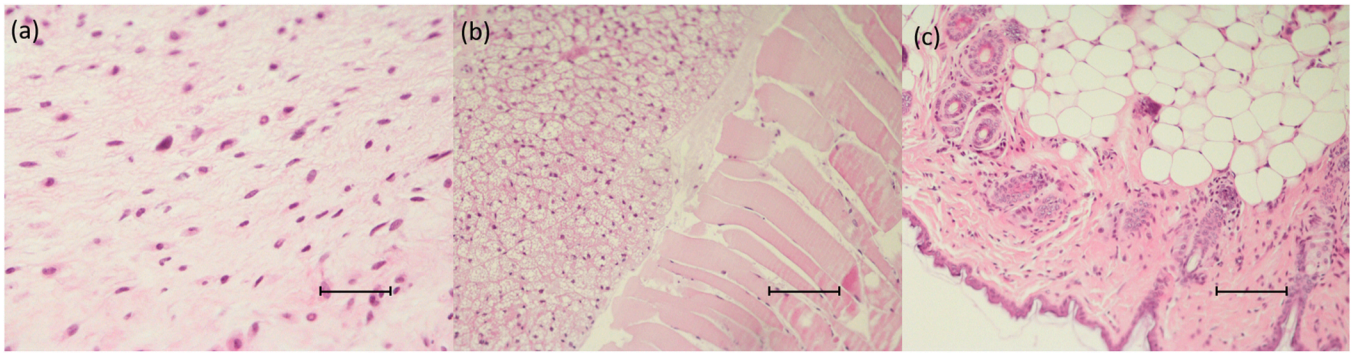

Fig. 14. Connective tissue capsule surrounding the implant (a). In the tissue adjacent to the implant, skeletal muscle fibers as well as brown and white adipose tissue are present (b). Skin samples show a thin epidermis and dermis, with visible hair follicles and subcutaneous adipose tissue (c). (H&E staining; original magnification: × 100 (a), × 40 (b, c); scale bars represent 200 µm (a) and 500 µm (b, c).

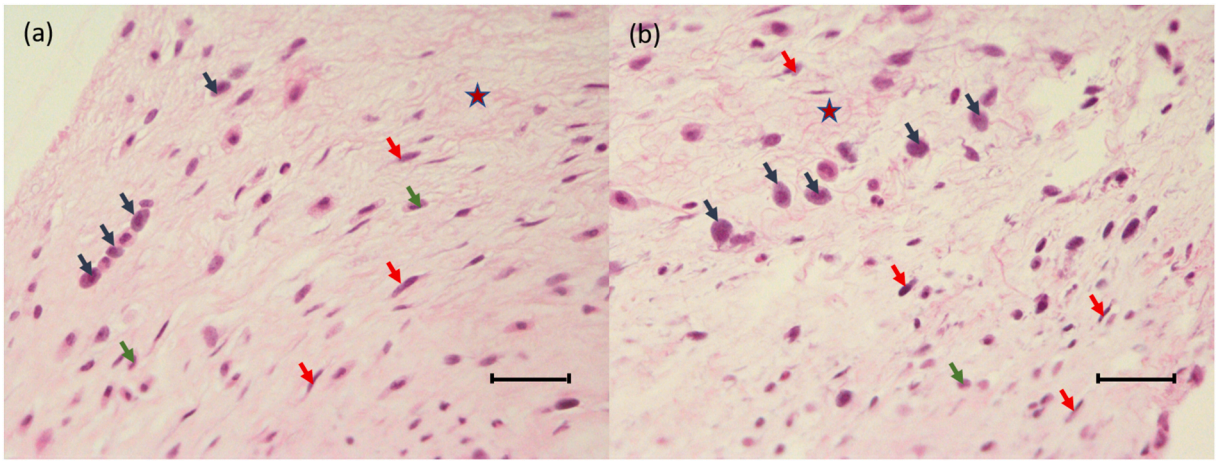

Fig. 15. Connective tissue capsules surrounding (a) Ti–6Al–4V and (b) Ti–6Al–4V–4Cu implants are composed of loose connective tissue-containing macrophages (↘), fibroblasts (↘), granulocytes (↘), and scattered collagen fibers (↘). Macrophages with dusty black cytoplasm (★) are present in both groups, with no apparent differences in their density. (H&E staining; original magnification: × 400; scale bars represent 50 µm).

Ti_2Cu phases. Electrochemical testing in simulated physiological conditions demonstrated high corrosion resistance, comparable to that of a Cu-free alloy, yet identified features related to the Cu-containing phase. *In vivo* subcutaneous implantation in mice revealed no signs of systemic toxicity, inflammation, or abnormal histology, with stable physiological parameters and serum metal ion concentrations over 56 days. Together, these findings confirm the *in vivo* biocompatibility and material stability of the powder DED-LB process based additive manufacturing of Ti–6Al–4V–4Cu alloy, supporting its potential for biomedical applications requiring both corrosion resistance and biological safety. Future work will address its antibacterial properties under infected conditions and evaluate performance in bone or dental implantation models to

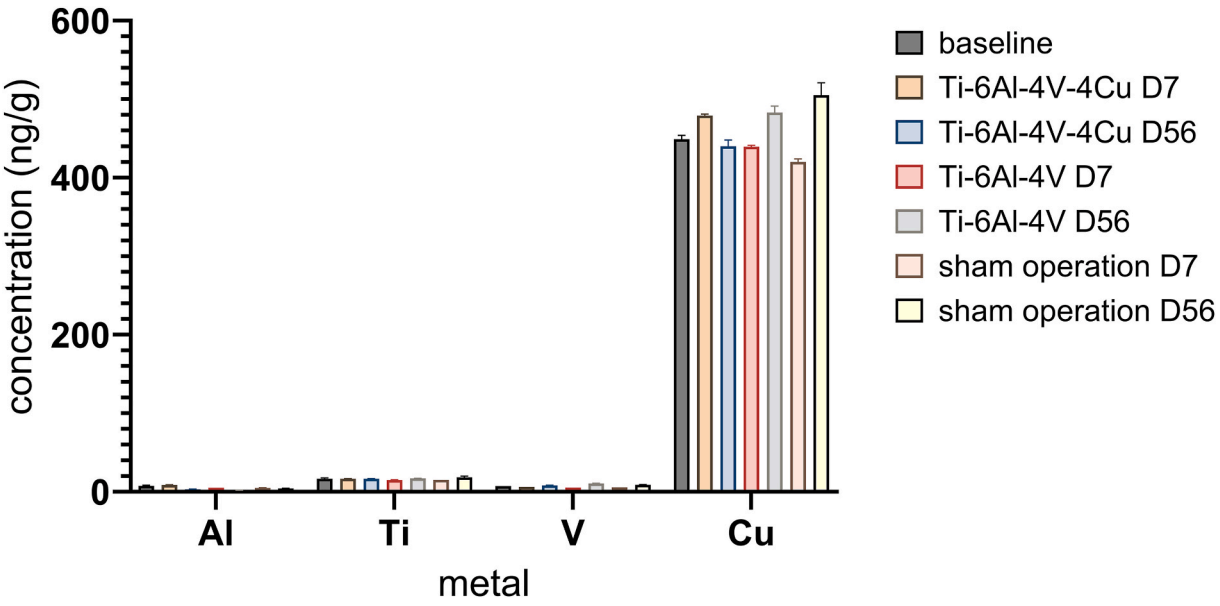

Fig. 16. Serum concentrations of metal ions (Cu, Al, V, Ti) measured by ICP-MS on Days 7 and 56 in baseline, sham-operated, Ti–6Al–4V, and Ti–6Al–4V–4Cu groups.

explore its dual functionality as a structural and antimicrobial implant material.

Data availability statement

The data supporting this study's findings are available on request from the corresponding authors.

Declaration of generative AI and AI-assisted technologies in the writing process

During the preparation of this work, the authors used OpenAI's ChatGPT (version GPT-4, July 2025) and Grammarly (v1.2.177.1709) for language editing during manuscript preparation. After using this tool/service, the authors reviewed and edited the content as needed and take full responsibility for the content of the publication.

Funding sources

The authors acknowledge the Slovenian Research and Innovation Agency (ARIS) for the funding of the project » Antibacterial alloys: Development by additive 3D manufacturing, characterization and clinical applications«, acronym BIOAD, https://bioad.ijs.si/(grant No. J7-4639) and core funding (grants No. P2-0393, No. P1-0134, No. P2-0241, and P4-0220).

Declaration of competing interest

The authors declare that they have no known competing financial interests or personal relationships that could have appeared to influence the work reported in this paper.

Acknowledgements

The authors acknowledge the technical assistance of the Laboratory for Cutting at the Faculty of Mechanical Engineering, University of Ljubljana, for machining of disc samples from the DED-LB-fabricated Ti–6Al–4V–4Cu alloy walls. XRD analysis was conducted at the National Institute of Chemistry in Ljubljana by Prof. Nataša Zabukovec Logar. The authors acknowledge the use of SEM/EDS equipment at the Center for Electron Microscopy and Microanalysis (CEMM) of the Jožef Stefan Institute and the Nanocenter Center of Excellence for Nanoscience and Nanotechnology. The authors acknowledge Dr Chenyang Xie of the Department of Physical and Organic Chemistry at the Jožef Stefan Institute for the processing of the SEM image using the ImageJ programme and the technical assistance of Ms Ana Jakopič for support in the mouse experiments conducted at the Biotechnical Faculty.

Appendix A. Supplementary data

Supplementary data to this article can be found online at https://doi.org/10.1016/j.jmrt.2025.10.151.

References

[1] Li S, Liu H, Siddiqui MA, Li Y, Wang H, Zhang SY, et al. Corrosion behavior and biofunctions of the ultrafine-grained Ti6Al4V-5Cu alloy with a dual-phase honeycomb shell structure in simulated body fluid. ACS Biomater Sci Eng 2023;9:2362–75. https://doi.org/10.1021/acsbiomaterials.2c01316.
[2] Bocchetta P, Chen LY, Tardelli JDC, Dos Reis AC, Almeraya-Calderón F, Leo P. Passive layers and corrosion resistance of biomedical Ti-6Al-4V and β-Ti alloys. Coatings 2021;11:1–33. https://doi.org/10.3390/coatings11050487.
[3] Liu S, Shin YC. Additive manufacturing of Ti6Al4V alloy: a review. Mater Des 2019;164:8–12. https://doi.org/10.1016/j.matdes.2018.107552.
[4] Hengel IAJ van, Dijk B van, Khashayar M, Duyvenbode JFFH van, Nurmohamed FRHA, Leeflang MA, et al. In vivo prevention of implant-associated infections caused by antibiotic-resistant bacteria through biofunctionalization of additively manufactured porous titanium. J Funct Biomater 2023;14:1–20. https://doi.org/10.3390/jfb14100520.
[5] Yu B, Ren Y, Zeng Y, Ma W, Morita K, Zhan S, et al. Recent progress in high-entropy alloys: a focused review of preparation processes and properties. J Mater Res Technol 2024;29:2689–719. https://doi.org/10.1016/j.jmrt.2024.01.246.
[6] Zhuang Y, Zhang S, Yang K, Ren L, Dai K. Antibacterial activity of copper-bearing 316L stainless steel for the prevention of implant-related infection. J Biomed Mater Res Part B Appl Biomater 2020;108:484–95. https://doi.org/10.1002/jbm.b.34405.
[7] Zhuang Y, Ren L, Zhang S, Wei X, Yang K, Dai K. Antibacterial effect of a copper-containing titanium alloy against implant-associated infection induced by methicillin-resistant Staphylococcus aureus. Acta Biomater 2021;119:472–84. https://doi.org/10.1016/j.actbio.2020.10.026.
[8] Li Y, Lu Y, Qiu B, Ze Y, Li P, Du Y, et al. Copper-containing titanium alloys promote angiogenesis in irradiated bone through releasing copper ions and regulating immune microenvironment. Biomater Adv 2022;139:1–14. https://doi.org/10.1016/j.bioadv.2022.213010.
[9] Liu R, Tang Y, Zeng L, Zhao Y, Ma Z, Sun Z, et al. In vitro and in vivo studies of antibacterial copper-bearing titanium alloy for dental application. Dent Mater 2018;34:1112–26. https://doi.org/10.1016/j.dental.2018.04.007.

[10] Ren L, Ma Z, Li M, Zhang Y, Liu W, Liao Z, et al. Antibacterial properties of Ti-6Al-4V-xCu alloys. J Mater Sci Technol 2014;30:699–705. https://doi.org/10.1016/j.jmst.2013.12.014.
[11] Krakhmalev P, Yadroitsev I, Yadroitsava I, Smidt O de. Functionalization of biomedical Ti6Al4V via in situ alloying by Cu during laser powder bed fusion manufacturing. Materials 2017;10:1–14. https://doi.org/10.3390/ma10101154.
[12] Wang X, Liu W, Jiang C, Pan P, Chen T, Zhang X, et al. Research progress on the osteogenic properties of tantalum in the field of medical implant materials. J Mater Res Technol 2024;30:1706–15. https://doi.org/10.1016/j.jmrt.2024.03.200.
[13] Mirabad HM, Akbarpour MR, Gazani F, Chadegani AA, Khezri I, Mirzamohammad A, et al. The microstructure-mechanical property relationships in Ti–Cu alloys for biomedical applications: a review. J Mater Res Technol 2025;37:3155–81. https://doi.org/10.1016/j.jmrt.2025.06.184.
[14] Ma Z, Ren L, Liu R, Yang K, Zhang Y, Liao Z, et al. Effect of heat treatment on Cu distribution, antibacterial performance and cytotoxicity of Ti-6Al-4V-5Cu alloy. J Mater Sci Technol 2015;31:723–32. https://doi.org/10.1016/j.jmst.2015.04.002.
[15] Wu JH, Chen KK, Chao CY, Chang YH, Du JK. Effect of Ti2Cu precipitation on antibacterial property of Ti-5Cu alloy. Mater Sci Eng C 2020;108:1–8. https://doi.org/10.1016/j.msec.2019.110433.
[16] Zhang E, Li F, Wang H, Liu J, Wang C, Li M, et al. A new antibacterial titanium-copper sintered alloy: preparation and antibacterial property. Mater Sci Eng C 2013;33:4280–7. https://doi.org/10.1016/j.msec.2013.06.016.
[17] Huber F, Papke T, Scheitler C, Hanrieder L, Merklein M, Schmidt M. In situ formation of a metastable β-Ti alloy by laser powder bed fusion (L-PBF) of vanadium and iron modified Ti-6Al-4V. Metals 2018;8:1–9. https://doi.org/10.3390/met8121067.
[18] Li K, Yang J, Yi Y, Liu X, Liu Y, Zhang LC, et al. Enhanced strength-ductility synergy and mechanisms of heterostructured Ti6Al4V-Cu alloys produced by laser powder bed fusion. Acta Mater 2023;256:1–16. https://doi.org/10.1016/j.actamat.2023.119112.
[19] Goettgens VS, Kaserer L, Braun J, Busch R, Berthold L, Patzig C, et al. Microstructural evolution and mechanical properties of Ti-6Al-4V in situ alloyed with 3.5 wt.% Cu by laser powder bed fusion. Materialia 2023;32:1–11. https://doi.org/10.1016/j.mtla.2023.101928.
[20] Guo S, Lu Y, Wu S, Liu L, He M, Xu X, et al. Preliminary study on the corrosion resistance, antibacterial activity and cytotoxicity of selective-laser-melted Ti6Al4V-xCu alloys. Mater Sci Eng C 2017;72:631–40. https://doi.org/10.1016/j.msec.2016.11.126.
[21] Vilardell AM, Yadroitsev I, Yadroitsava I, Albu M, Takata N, Kobashi M, et al. Manufacturing and characterization of in-situ alloyed Ti6Al4V(ELI)-3 at.% Cu by laser powder bed fusion. Addit Manuf 2020;36:1–14. https://doi.org/10.1016/j.addma.2020.101436.
[22] Ciliveri S, Bandyopadhyay A. Understanding the influence of alloying elements on the print quality of powder bed fusion-based metal additive manufacturing: Ta and Cu addition to Ti alloy. Virtual Phys Prototyp 2023;18:1–16. https://doi.org/10.1080/17452759.2023.2248464.
[23] Wang Q, Zhang K, Niu W. Microstructural characteristic and mechanical properties of titanium-copper alloys in-situ fabricated by selective laser melting. J Alloys Compd 2021;885:1–11. https://doi.org/10.1016/j.jallcom.2021.161032.
[24] Wei C, Li L. Recent progress and scientific challenges in multi-material additive manufacturing via laser-based powder bed fusion. Virtual Phys Prototyp 2021;16:347–71. https://doi.org/10.1080/17452759.2021.1928520.
[25] Nazir A, Gokcekaya O, Md Masum Billah K, Ertugrul O, Jiang J, Sun J, et al. Multi-material additive manufacturing: a systematic review of design, properties, applications, challenges, and 3D printing of materials and cellular metamaterials. Mater Des 2023;226:1–36. https://doi.org/10.1016/j.matdes.2023.111661.
[26] Chen LY, Liang SX, Liu Y, Zhang LC. Additive manufacturing of metallic lattice structures: unconstrained design, accurate fabrication, fascinated performances, and challenges. Mater Sci Eng R Reports 2021;146:1–56. https://doi.org/10.1016/j.mser.2021.100648.
[27] Li J, Zhang D, Chen X, Xu D, Qiu D, Wang F, et al. Laser directed energy deposited, ultrafine-grained functional titanium-copper alloys tailored for marine environments: antibacterial and anti-microbial corrosion studies. J Mater Sci Technol 2023;166:21–33. https://doi.org/10.1016/j.jmst.2023.05.020.
[28] Wang X, Zhang LJ, Ning J, Na SJ. Effect of Cu-induced eutectoid transformation on microstructure and mechanical properties of Ti–6Al–4V alloy by laser wire deposition. Mater Sci Eng A 2022;833:1–13. https://doi.org/10.1016/j.msea.2021.142316.
[29] Chen Y, Zhang X, Parvez MM, Liou F. A review on metallic alloys fabrication using elemental powder blends by laser powder directed energy deposition process. Materials 2020;13:1–19. https://doi.org/10.3390/MA13163562.
[30] Feenstra DR, Banerjee R, Fraser HL, Huang A, Molotnikov A, Birbilis N. Critical review of the state of the art in multi-material fabrication via directed energy deposition. Curr Opin Solid State Mater Sci 2021;25:1–12. https://doi.org/10.1016/j.cossms.2021.100924.
[31] Chen LY, Qin P, Zhang L, Zhang LC. An overview of additively manufactured metal matrix composites: preparation, performance, and challenge. Int J Extrem Manuf 2024;6:1–44. https://doi.org/10.1088/2631-7990/ad54a4.
[32] Zhang D, Qiu D, Gibson MA, Zheng Y, Fraser HL, StJohn DH, et al. Additive manufacturing of ultrafine-grained high-strength titanium alloys. Nature 2019;576:91–5. https://doi.org/10.1038/s41586-019-1783-1.
[33] Kim TW, Kim DH, Cho YT, Lee CM. Manufacturing high strength Ti alloy with in-situ Cu alloying via directed energy deposition and evaluation of material properties. J Mater Res Technol 2024;28:1810–23. https://doi.org/10.1016/j.jmrt.2023.12.115.
[34] Milošev I. From in vitro to retrieval studies of orthopedic implants. Corrosion 2017;73:1496–509. https://doi.org/10.5006/2576.
[35] Chandramohan P, Bhero S, Obadele BA, Olubambi PA. Laser additive manufactured Ti–6Al–4V alloy: tribology and corrosion studies. Int J Adv Manuf Technol 2017;92:3051–61. https://doi.org/10.1007/s00170-017-0410-2.
[36] Fojt J, Fousova M, Jablonska E, Joska L, Hybasek V, Pruchova E, et al. Corrosion behaviour and cell interaction of Ti-6Al-4V alloy prepared by two techniques of 3D printing. Mater Sci Eng C 2018;93:911–20. https://doi.org/10.1016/j.msec.2018.08.066.
[37] Bozkurt YB, Kavasoğlu YS, Atik B, Kovacı H, Uzun Y, Çelik A. Comparison study of corrosion behavior for chitosan coated Ti6Al4V alloy produced by selective laser melting and forging. Prog Org Coatings 2023;182:1–10. https://doi.org/10.1016/j.porgcoat.2023.107655.
[38] Cui YW, Chen LY, Chu YH, Zhang L, Li R, Lu S, et al. Metastable pitting corrosion behavior and characteristics of passive film of laser powder bed fusion produced Ti–6Al–4V in NaCl solutions with different concentrations. Corros Sci 2023;215:1–14. https://doi.org/10.1016/j.corsci.2023.111017.
[39] Toptan F, Alves AC, Carvalho Ó, Bartolomeu F, Pinto AMP, Silva F, et al. Corrosion and tribocorrosion behaviour of Ti6Al4V produced by selective laser melting and hot pressing in comparison with the commercial alloy. J Mater Process Technol 2019;266:239–45. https://doi.org/10.1016/j.jmatprotec.2018.11.008.
[40] Fojt J, Hybášek V, Kačenka Z, Průchová E. Influence of surface finishing on corrosion behaviour of 3d printed TiAlV alloy. Metals 2020;10:1–11. https://doi.org/10.3390/met10111547.
[41] Chen LY, Zhang HY, Zheng C, Yang HY, Qin P, Zhao C, et al. Corrosion behavior and characteristics of passive films of laser powder bed fusion produced Ti–6Al–4V in dynamic Hank's solution. Mater Des 2021;208:109907. https://doi.org/10.1016/j.matdes.2021.109907.
[42] Bai C, Li P, Gang T, Li J, Wei M, Huang Y, et al. Influence of processing technology on electrochemical corrosion behavior of Ti-6Al-4V alloys. Corrosion 2021;77:402–12. https://doi.org/10.5006/3490.
[43] Cui YW, Chen LY, Qin P, Li R, Zang Q, Peng J, et al. Metastable pitting corrosion behavior of laser powder bed fusion produced Ti-6Al-4V in Hank's solution. Corros Sci 2022;203:110333. https://doi.org/10.1016/j.corsci.2022.110333.
[44] Zhang H, Qin W, Man C, Cui H, Kong D, Cui Z, et al. Effect of heat treatment on microstructure and corrosion behavior of Ti6Al4V fabricated by laser beam powder bed fusion. Corros Sci 2022;209:1–20. https://doi.org/10.1016/j.corsci.2022.110789.
[45] Leban MB, Kosec T, Finšgar M. Corrosion characterization and ion release in SLM-manufactured and wrought Ti6Al4V alloy in an oral environment. Corros Sci 2022;209:1–15. https://doi.org/10.1016/j.corsci.2022.110716.
[46] Bajt Leban M, Kosec T, Finšgar M. The corrosion resistance of dental Ti6Al4V with differing microstructures in oral environments. J Mater Res Technol 2023;27:1982–95. https://doi.org/10.1016/j.jmrt.2023.10.082.
[47] Dehnavi V, Henderson JD, Dharmendra C, Amirkhiz BS, Shoesmith DW, Noël JJ, et al. Corrosion behaviour of electron beam melted Ti6Al4V: effects of microstructural variation. J Electrochem Soc 2020;167:1–10. https://doi.org/10.1149/1945-7111/abb9d1.
[48] Shalnova SA, Gushchina MO, Strekalovskaya DA, Alekseeva EL, Klimova-Korsmik OG. Electrochemical properties of the heat-treated Ti-6Al-4V alloy manufactured by direct energy deposition. J Alloys Compd 2022;899:1–8. https://doi.org/10.1016/j.jallcom.2021.163226.
[49] Milošev I, Rodič P, Kapun B, Sačer D, Nair A, Kramar D, et al. Composition , microstructure and corrosion resistance of DED-LB additively manufactured Ti – 6Al – 4V alloy : Comparison with wrought alloy. J Alloys Compd 2025;1033:1–19. https://doi.org/10.1016/j.jallcom.2025.181280.
[50] Liu H, Shi L, Liu H, Ren L, Yang K. Corrosion behavior of laser powder bed fusion prepared antibacterial Cu-bearing titanium alloy. Mater Lett 2023;331:1–4. https://doi.org/10.1016/j.matlet.2022.133496.
[51] Liu H, Zhang X, Shi L, Hong Y, Yao H, Ren L, et al. Effect of Cu content on the properties of laser powder bed fused biomedical titanium alloys. J Mater Res Technol 2024;30:8992–8. https://doi.org/10.1016/j.jmrt.2024.05.216.
[52] Wang X, Qin P, Chen LY, Sun H, Zhang LC. Corrosion behavior and mechanisms of the heat-treated Ti5Cu produced by laser powder bed fusion. Corros Sci 2023;221:1–15. https://doi.org/10.1016/j.corsci.2023.111336.
[53] Liu H, Liu H, Zhang S, Wang H, Wei X, Ren L, et al. Metastable pitting corrosion behavior of laser powder bed fusion produced Ti6Al4V-Cu in 3.5% NaCl solution. Corros Sci 2023;223:1–12. https://doi.org/10.1016/j.corsci.2023.111452.
[54] Li L, Chen Y, Lu Y, Qin S, Huang G, Huang T, et al. Effect of heat treatment on the corrosion resistance of selective laser melted Ti6Al4V3Cu alloy. J Mater Res Technol 2021;12:904–15. https://doi.org/10.1016/j.jmrt.2021.03.041.
[55] Ju J, Zan R, Shen Z, Wang C, Peng P, Wang J, et al. Remarkable bioactivity, biotribological, antibacterial, and anti-corrosion properties in a Ti-6Al-4V-xCu alloy by laser powder bed fusion for superior biomedical implant applications. Chem Eng J 2023;471:1–15. https://doi.org/10.1016/j.cej.2023.144656.
[56] Zhang E, Li S, Ren J, Zhang L, Han Y. Effect of extrusion processing on the microstructure, mechanical properties, biocorrosion properties and antibacterial properties of Ti-Cu sintered alloys. Mater Sci Eng C 2016;69:760–8. https://doi.org/10.1016/j.msec.2016.07.051.
[57] Liu H, Liu R, Ullah I, Zhang S, Sun Z, Ren L, et al. Rough surface of copper-bearing titanium alloy with multifunctions of osteogenic ability and antibacterial activity. J Mater Sci Technol 2020;48:130–9. https://doi.org/10.1016/j.jmst.2019.12.019.
[58] Xin C, Wang N, Chen Y, He B, Zhao Q, Chen L, et al. Biological corrosion behaviour and antibacterial properties of Ti-Cu alloy with different Ti2Cu morphologies for dental applications. Mater Des 2022;215:1–11. https://doi.org/10.1016/j.matdes.2022.110540.

[59] Zhao X, Hu J, Nie J, Chen D, Qin G, Zhang E. Enhanced antibacterial activity, corrosion resistance and endothelialization potential of Ti-5Cu alloy by oxygen and nitrogen plasma-based surface modification. J Mater Sci Technol 2024;168:250–64. https://doi.org/10.1016/j.jmst.2023.04.076.
[60] Kolawole SK, Hai W, Zhang S, Sun Z, Siddiqui MA, Ullah I, et al. Preliminary study of microstructure, mechanical properties and corrosion resistance of antibacterial Ti-15Zr-xCu alloy for dental application. J Mater Sci Technol 2020;50:31–43. https://doi.org/10.1016/j.jmst.2020.03.003.
[61] Wang X, Dong H, Liu J, Qin G, Chen D, Zhang E. In vivo antibacterial property of Ti-Cu sintered alloy implant. Mater Sci Eng C 2019;100:38–47. https://doi.org/10.1016/j.msec.2019.02.084.
[62] Ren L, Wong HM, Yan CH, Yeung KWK, Yang K. Osteogenic ability of Cu-bearing stainless steel. J Biomed Mater Res Part B Appl Biomater 2015;103:1433–44. https://doi.org/10.1002/jbm.b.33318.
[63] Xu D, Qian J, Guan X, Ren L, Yang K, Huang X, et al. Copper-Containing alloy as immunoregulatory material in bone regeneration via mitochondrial oxidative stress. Front Bioeng Biotechnol 2021;8:1–12. https://doi.org/10.3389/fbioe.2020.620629.
[65] Wang P, Xu X, Gu G, Guo Q, Rao Y, Yang K, et al. Inhibition effect of copper-bearing metals on arterial neointimal hyperplasia via the AKT/Nrf2/ARE pathway in vitro and in vivo. Regen Biomater 2024;11:1–15. https://doi.org/10.1093/rb/rbae042.
[66] Zhou C, Li H-F, Yin Y-X, Shi Z-Z, Li T, Feng X-Y, et al. Long-term in vivo study of biodegradable Zn-Cu stent: a 2-year implantation evaluation in porcine coronary artery. Acta Biomater 2019;97:657–70. https://doi.org/10.1016/j.actbio.2019.08.012.
[67] Song Y, Hu Q, Liu S, Wang Y, Jia L, Hu X, et al. 3D printed biomimetic composite scaffolds with sequential releasing of copper ions and dexamethasone for cascade regulation of angiogenesis and osteogenesis. Chem Eng J 2024;496:1–16. https://doi.org/10.1016/j.cej.2024.153662.
[68] Zhang M, Zhu L, Wang J, Ye N, Dai S, Yu S, et al. Surface modification of biomedical metals by double glow plasma surface alloying technology: a review of recent advances. J Mater Res Technol 2023;24:3423–52. https://doi.org/10.1016/j.jmrt.2023.04.003.
[69] Vidergar A, Jeromen A, Govekar E. Influence of the laser-beam intensity distribution on the performance of directed energy deposition of an axially fed metal powder. J Mater Process Technol 2024;327:1–16. https://doi.org/10.1016/j.jmatprotec.2024.118360.
[70] Bowen P. Particle size distribution measurement from millimeters to nanometers and from rods to platelets. J Dispers Sci Technol 2002;23:631–62. https://doi.org/10.1081/DIS-120015368.
[71] Milošev I, Sačer D, Kapun B, Rodič P. The effect of metallographic preparation on the surface characteristics and corrosion behaviour of Ti-6Al-4V alloy in simulated physiological solutions. J Electrochem Soc 2024;171:1–15. https://doi.org/10.1149/1945-7111/ad8e89.
[72] Zoller SD, Hegde V, Burke ZDC, Park HY, Ishmael CR, Blumstein GW, et al. Evading the host response: staphylococcus “hiding” in cortical bone canalicular system causes increased bacterial burden. Bone Res 2020;8:1–11. https://doi.org/10.1038/s41413-020-00118-w.
[73] Langford DJ, Bailey AL, Chanda ML, Clarke SE, Drummond TE, Echols S, et al. Coding of facial expressions of pain in the laboratory mouse. Nat Methods 2010;7:447–9. https://doi.org/10.1038/nmeth.1455.
[74] DebRoy T, Wei HL, Zuback JS, Mukherjee T, Elmer JW, Milewski JO, et al. Additive manufacturing of metallic components – process, structure and properties. Prog Mater Sci 2018;92:112–224. https://doi.org/10.1016/j.pmatsci.2017.10.001.
[75] Sengodan VC, Doddihithlu S. Analysis of hematological metal element levels in orthopedic patients with implants. J Nat Sci Biol Med 2020;11:17–20. https://doi.org/10.4103/jnsbm.JNSBM_120_19.
[76] Kram W, Rebl H, Cruz JE de la, Haag A, Renner J, Epting T, et al. Interactive effects of copper-doped urological implants with tissue in the urinary tract for the inhibition of cell adhesion and encrustation in the animal model rat. Polymers 2022;14:1–21. https://doi.org/10.3390/polym14163324.
[77] https://doi.org/10.1016/j.bioactmat.2021.05.053.